Draft version November 16, 2021
Preprint typeset using LaTeX style emulateapj v. 12/16/11

GRB170817A ASSOCIATED WITH GW170817: MULTIFREQUENCY OBSERVATIONS AND MODELING OF PROMPT GAMMA-RAY EMISSION

A.S. Pozanenko[1,2,3], M.V. Barkov[4,5], P.Yu. Minaev[1], A.A. Volnova[1], E.D. Mazaeva[1], A.S. Moskvitin[6], M.A. Krugov[7], V.A. Samodurov[2,8], V.M. Loznikov[1], and M.Lyutikov[4]

[1]Space Research Institute, 84/32 Profsoyuznaya Street, Moscow 117997, Russia
[2]National Research University Higher School of Economics, Myasnitskaya 20, 101000, Moscow, Russia
[3]National Research Nuclear University MEPhI (Moscow Engineering Physics Institute), Kashirskoe shosse, 31, 115409 Moscow, Russia
[4]Department of Physics and Astronomy, Purdue University, 525 Northwestern Avenue, West Lafayette, IN 47907-2036, USA
[5]Astrophysical Big Bang Laboratory, RIKEN, 2-1 Hirosawa, Wako, Saitama 351-0198, Japan
[6]Special Astrophysical Observatory of Russian Academy of Sciences, Nizhniy Arkhyz, 369167, Russia
[7]Fesenkov Astrophysical Institute, Almaty, 050020, Kazakhstan
[8]Pushchino Radio Astronomy Observatory ASC LPI, Pushchino, Russia

Draft version November 16, 2021

Abstract

We present details of our observational campaigns of electromagnetic transients associated with GW170817/GRB170817A using optical telescopes of Chilescope observatory and Big Scanning Antenna (BSA) of Pushchino Radio Astronomy Observatory at 110 MHz. The Chilescope observatory detected an optical transient of $\sim 19^m$ on the third day in the outskirts of the galaxy NGC 4993; we continued observations following its rapid decrease. We put an upper limit of 1.5×10^4 Jy on any radio source of duration 10–60 s which may be associated with GW170817/GRB170817A. The prompt gamma-ray emission consists of two distinctive components - a hard short pulse delayed by ~ 2 seconds with respect to the LIGO signal and softer thermal pulse with $T \sim 10$ keV lasting for another ~ 2 seconds. The appearance of thermal component at the end of the burst is uncharacteristic for GBRs. Both the hard and the soft components do not satisfy the Amati relation, making GRB170817A distinctively different from other short GRBs. Based on gamma-ray and optical observations we develop a model of prompt high-energy emission associated with GRB170817A. The merger of two neutron stars create an accretion torus of $\sim 10^{-2} M_\odot$, which supplies the black hole with magnetic flux and confines the Blandford-Znajek-powered jet. We associate the hard prompt spike with the quasi-spherical break-out of the jet from the disk wind. As the jet plows through the wind with sub-relativistic velocity, it creates a radiation dominated shock that heats the wind material to tens of keV, producing the soft thermal component. After the break out the continuing jet regains collimation so that its emission, as well as early afterglows, is beamed away from the observer. The model explains both the off-axis viewing geometry and observations of the prompt emission.

Subject headings: gravitational waves, gamma-ray burst: individual (GRB170817A), accretion, accretion disks, techniques: photometric, radio continuum: general

1. INTRODUCTION

On August 17, 2017 at 12:41:04 UTC the LIGO-Hanford detector triggered the gravitational-wave (GW) transient GW170817 (LIGO Scientific Collaboration & Virgo Collaboration 2017a). The GW signal was also found in the data of other LIGO and Virgo detectors and was consistent with a binary neutron star system coalescence. Two seconds later (UTC 2017-08-17 12:41:06) GRB 170817A was registered by GBM/Fermi (Goldstein et al. 2017; Connaughton et al. 2017; Goldstein et al. 2017) and SPI-ACS/INTEGRAL (Savchenko et al. 2017,?) experiments. The GRB 170817A localization area includes the much less localization region of GW170817. A search of the optical counterpart started immediately and was carried out by a large number of ground-based facilities (LIGO Scientific Collaboration et al. 2017).

2. OBSERVATIONS

2.1. *Chronology*

The optical transient corresponding to the GW170817 and GRB170817A was discovered independently by several observatories. The first team to discover and report the detection of the optical counterpart was The One-Meter, Two-Hemisphere (1M2H) group. They detected a bright uncatalogued source within the halo of the galaxy NGC4993 in their i-band image obtained on Aug. 17, 2017 23:33 UTC with the 1m Swope telescope at Las Campanas Observatory in Chile and the source was labeled Swope Supernova Survey 2017a (SSS17a; Coulter et al. 2017, notice time Aug 18, 2017 01:05 UTC). SSS17a (now with the IAU designation AT2017gfo) had coordinates RA(J2000.0) = $13^h09^m48\overset{s}{.}085 \pm 0.018$, Dec(J2000.0) = $-23°22'53\overset{''}{.}343 \pm 0.218$ and was located at a projected distance of $10\overset{''}{.}6$ from the center of NGC 4993, an early-type galaxy at a distance of $\simeq 40 Mpc$. Hereafter we refer to the optical counterpart as OT.

The Distance Less Than 40Mpc survey (DLT40; Tartaglia et al. 2017, in prep.) obtained their first image of NGC4993 region on Aug 17, 2017 23:50 UTC and independently detected the transient, automatically labeled DLT17ck (Yang et al. 2017, ; notice time Aug 18,

01:41 UTC).

MASTER-OAFA robotic telescope (Lipunov et al. 2010) observed the region including NGC 4993 on Aug 17 23:59 UTC, and the automated software independently detected the transient labeled MASTER OT J130948.10-232253.3 (Lipunov et al. 2017, notice time Aug 18 05:38 UTC).

Visible and Infrared Survey Telescope for Astronomy (VISTA) also observed the transient SSS17a/DLT17ck/MASTER OT J130948.10-232253.3 in the infrared light on Aug 18, 00:10 UT (Tanvir & Levan 2017, notice time Aug 18, 05:04 UTC).

Las Cumbres Observatory (LCO; Brown et al. 2013) surveys started observations of the Fermi localization region immediately after the corresponding GCN circular distribution. Approximately 5 h later, when the LIGO-Virgo localization map was issued, the observations were switched to the priority list of galaxies (Dalya et al. 2016). On Aug 18 00:15 UTC, a new transient near NGC 4993 was detected at the position corresponding to the OT (Arcavi et al. 2017, notice time Aug 18, 04:07 UTC).

The team of DECam on the 4-meter telescope of Cerro Tololo Inter-American Observatory independently visually detected the new source north and east of NGC 4993 in the frame taken on Aug 18, 00:42 UTC (Allam et al. 2017, notice time Aug 18, 01:15 UTC).

We started observations of the the error box of GW170817 (LIGO/Virgo trigger G298048) on Aug 17 23:17:16 UTC in a clear filter (Pozanenko et al. 2017a, notice time Aug 18, 14:24 UTC). Simultaneously we started mosaic observations of GRB 170817A (von Kienlin et al. 2017). The observations ended $\sim$ 5 minutes earlier than the GCN circular from Swope about the discovery of the transient was distributed. The location of the NGC 4993 was out of the covered fields of our first observational set. Details of the mosaic observations are presented in Appendix A.3. We continued our observations next days and clearly detected the plateau phase and rapid decay of the OT.

2.2. *SSS17a observations*

We started to observe the optical counterpart of the GW 170817 (LIGO Scientific Collaboration & Virgo Collaboration 2017a) labeled SSS17a (Coulter et al. 2017) on Aug. 19, 2017 at 23:30:33 UT taking several 180 s exposures in *Lum* filter with RC-1000 telescope of Chilescope observatory (see Section A.1; Pozanenko et al. 2017b). We clearly detected the source strongly contaminated by the host galaxy NGC 4993 background. We continued our observations on Aug. 20, 21 and 24, 2017 taking several 180 s exposures in each epoch (Pozanenko et al. 2017c,d). The weather conditions were satisfactory with a median seeing of 2 arcseconds. The seeing was not good for Chilean sky because the source was observed in the end of twilight when the atmosphere was not stable. The source was clearly detected in the stacked frames on Aug. 20 and 21 but faded on Aug. 24 below the detection limit over a host galaxy background. The optical transient SSS17a is shown in the Figure 1. The log of our observations is listed in the Table 1.

2.3. *Reduction and photometry*

All primary reduction of CCD images (bias and dark subtraction, flat-fielding) was performed using CCD-PROC task of IRAF software package[1]. The flux of the source is strongly affected by the host galaxy contribution, so the strategy of direct image subtraction was decided. Since the source was not detected in the stacked frame of the last observational epoch (Aug. 24), we chose this epoch as a template for the subtraction of the host galaxy. To align images of different observational epochs we used package ALIGN/IMAGE of ESO-MIDAS software[2] and `geomap` task of IRAF. The average image background was subtracted from all frames using median filter, and flux normalization for the image subtraction was performed using MAGNITUDE/CIRCLE task of ESO-MIDAS.

The photometry of the source after the host subtraction was made with PSF method using DAOPHOT

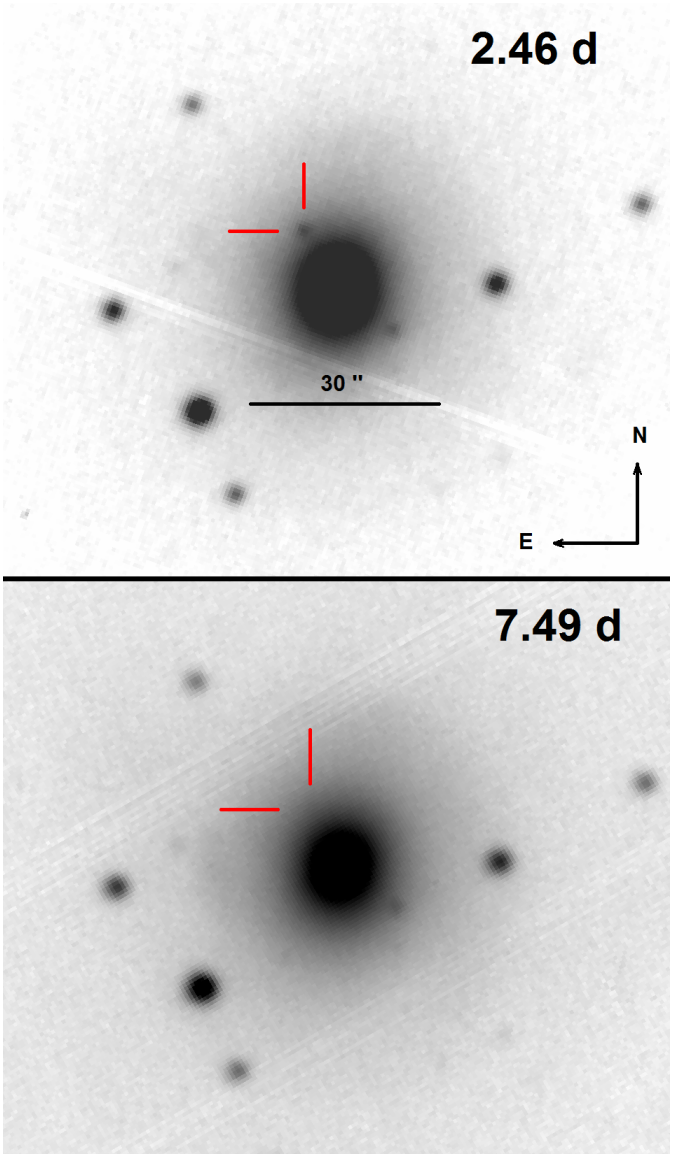

FIG. 1.— Imaging of the SSS17a / AT2017gfo in outskirts of the NGC 4993 galaxy with Chilescope/RC-1000 in two different epochs. Exposures of both frames are 10×180 seconds in the *Lum* filter.

[1] `http://iraf.noao.edu/`
[2] `http://www.eso.org/sci/software/esomidas/`

TABLE 1
LOG OF THE OPTICAL OBSERVATIONS AND PHOTOMETRY OF THE GW 170817. OBSERVATIONS IN LUM FILTER WERE CALIBRATED AGAINST USNO-B1.0 STARS, R2 MAGNITUDES. THE MAGNITUDES IN THE TABLE ARE NOT CORRECTED FOR THE GALACTIC EXTINCTION DUE TO THE REDDENING OF E(B-V) = 0.109 SCHLAFLY & FINKBEINER (2011) IN THE DIRECTION OF THE BURST.

Date	UT start	Exposure, s	Elapsed time, days	R mag.	error
2017-08-19	23:30:33	10×180	2.46157	19.12	0.06
2017-08-20	23:21:09	13×180	3.47840	20.04	0.08
2017-08-21	23:32:09	22×180	4.49409	20.14	0.12
2017-08-24	23:53:39	20×180	7.49278	> 21.0	–

package from IRAF software. The reference PSF stars were taken from the corresponding epoch background-subtracted flux-normalized stacked frame using tasks EXTRACT/IMAGE and INSERT/IMAGE of ESO-MIDAS software.

The resulting instrumental photometrical magnitudes was calibrated with the USNO-B1.0 catalog R2 magnitudes. After the accurate study of the field we chose 4 reference stars. The information about them is listed in the Table 2. The results of the photometry are presented in the Table 1.

2.4. *Optical light curve*

The light curve of the optical transient including published so far photometry in GCNs (LIGO Scientific Collaboration et al. 2017) in R, r and in Clear filters is presented the Figure 2. In the same figure we plot the optical afterglow of GRB 130603B (rescaled in both frequency and time) to the rest frame. We used parameters of the afterglow approximation ($Flux \sim t^{-2.72}$) after jet brake at about 0.4 *days* (Tanvir et al. 2013). The absolute calibration were taken in i-filter (Table 2 in Tanvir et al. 2013) which roughly corresponds to r-filter in the rest frame. For correct calculation of luminosity light curves of GRB 170817A and GRB 130603B we used Galactic extinction in the direction of the bursts, $E(B-V) = 0.109$ and $E(B-V) = 0.02$, correspondingly (Schlafly & Finkbeiner 2011). A host galaxy extinction was not taken into account. Surprisingly, the luminosity of kilonova releated to the GRB 130603B is roughly consistent with that of the GRB170817A kilonova component.

2.5. *BSA: radio observations at 110 MHz*

One of the most sensitive radio telescopes at the frequency of 110 MHz is a Big Scanning Antenna (BSA). BSA is the radio telescope of meridian type. The BSA observation is a continuous survey in multibeam mode in the frequency range of 109.0-111.5 MHz using 96 beams covering field of view from -8 and up to +42 degrees in *Declination* with a time resolution of 12.5 ms (Samodurov et al. 2017).

The OT position at the time of GW170817 trigger was 11.5 degrees above horizon at the BSA place, but out of the BSA diagram, i.e. 18 degrees lower in *Declination* and 12.8 minutes before the OT position. Would be a possible radio transient sufficiently bright one can detect it by side lobes of southern beams of the BSA. The bright sources such as Sun or Cygnus A (3C 405) are indeed registered in side lobes of BSA at distance of ±40 degrees with efficiency of $\sim 10^{-3}$ and at distance of ±10 degrees with efficiency of $\sim 10^{-2}$. We investigated all data set around the GW170817 trigger recorded with BSA.

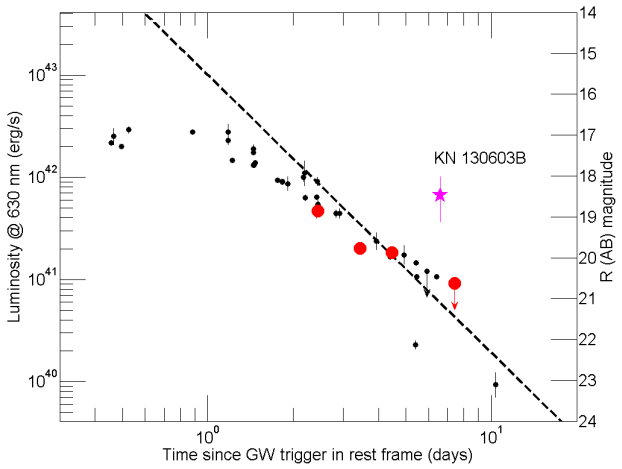

FIG. 2.— Light curve of the OT in units of stellar magnitude (right Y-axis) and total luminosity $L_{\rm iso}$ (left Y-axis). Red circles represent the observations made by Chilescope/RC-1000 telescope. The optical afterglow approximation of GRB130603B re-scaled to the rest frame is shown by the dashed line. The luminosity of a kilonova associated with GRB130603B is also shown (purple star). The luminosity is calculated from nIR data obtained in the F160W filter of HST (Tanvir et al. 2013).

The only one significant transient signal with a duration of 1.5 s centered at (UTC) 12:47:44.7 of about 100 Jy was detected in the southern beams at 109.273-111.148 MHz (see Figure 3). We mostly believe the signal has a non-astrophysical nature because of lack of a dispersion pattern which is specific for distant astrophysical objects such e.g. pulsars. We can place a conservative upper limit of 30 Jy (it is equivalent to $S/N > 10$) on a time scale of 10-60 sec for any astrophysical signal.

We can estimate intensity of possible astrophysical signal which can be detected by side lobes at the time of GW170817 trigger. The FWHM of side lobe along *Rightascension* in southern beams is about 5 minutes. The OT position was 2.5 of the FWHM at the trigger time of GW170817. Using a projection of BSA array toward the OT ($cos(79.5) = 0.18$) and side lobe efficiency $\sim 10^{-2}$ we estimate the upper limit on the transient radio signal from the position of the OT as 15000 Jy. The value can be converted in the upper limit of luminosity of a radio transient at the distance of the OT $E^{110\rm Mhz}_{\rm (iso)} < 5 \times 10^{40}$erg/s for a duration of the transient in the range of 10-60 seconds.

3. GRB 170817A PROMPT GAMMA-RAY DATA ANALYSIS

3.1. *SPI-ACS/INTEGRAL*

TABLE 2
Reference stars used for the photometrical reduction.

USNO-B1.0 ID	RA	Dec	USON-B1.0 R2 mag.	PanSTARRS r mag. (err)
0665-0279047	13:09:34.72	-23:24:45.9	17.26	17.474 (0.004)
0666-0290876	13:09:49.74	-23:20:34.6	16.51	16.812 (0.006)
0666-0290916	13:10:04.58	-23:20:47.8	17.23	17.466 (0.009)
0665-0279123	13:09:54.37	-23:25:34.3	16.89	17.224 (0.014)

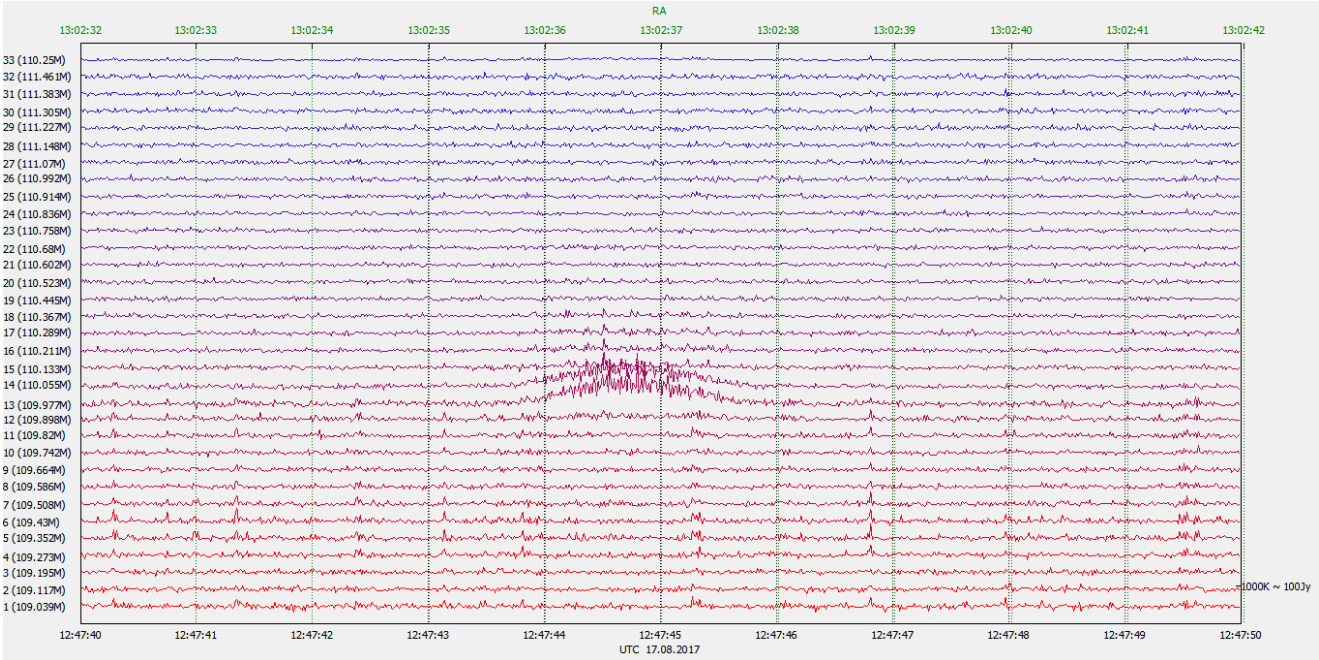

Fig. 3.— BSA observation at 109 - 110.25 MHz frequency channels (Y-axis) around the GW170817 trigger time (lower X-axis). In particular, in the shown beam toward $Dec.(J2000) = -4.82$ the nearly symmetric signal is visible at frequency channels from 109.898 and up to 110.367 MHz. The signal is visible in the southern beams and centered at (UTC) 12:47:44.7. This is the most powerful signal of about 100 Jy detected during 15 minutes since the GW170817 trigger. It has most probably an artificial origin.

A script (http://isdc.unige.ch/∼savchenk/spiacs-online/spiacs-ipnlc.pl) was used as the source of input SPI-ACS data.

GRB 170817A was detected in SPI-ACS at 4.5σ significance level. Background subtracted light curve of the burst in SPI-ACS data with time resolution of 0.2 s is presented on Figure 4 (panel d). The burst onset is delayed to GW trigger to $\simeq 2$ s. Third order polynomial model was used to fit background signal in time intervals (-118, -30) s and (300, 900) s (data before -118 s are not available). We found that for GRB 170817A there is the deviation of SPI-ACS count statistics from Poisson distribution with the factor of $\simeq 1.26$ (see e.g., Minaev et al. 2010; Minaev & Pozanenko 2017). Statistical uncertainties for SPI-ACS data were estimated with taking into account the factor of deviation.

The burst fluence calculated for (2, 3) s time interval since GW trigger is $F = (1.8 \pm 0.4) \times 10^3$ counts. The off-axis for GRB 170817A source from the satellite pointing axis is 105 deg, which is quite optimal for detection. In paper Viganò & Mereghetti (2009) was shown that 1 SPI-ACS count corresponds on average to $\approx 10^{-10}$erg/cm^2 in the (75, 1000) keV range, for directions orthogonal to the satellite pointing axis. Using the conversion factor we derive $F = (1.8 \pm 0.4) \times 10^{-7}$ erg/cm^2 in the (75, 1000) keV range for GRB 170817A. This value is in agreement with one estimated in Savchenko et al. (2017) using more complex method. The duration of the burst in SPI-ACS data is $T_{90}^{ACS} = 1.0 \pm 0.4$ s, which characterizes the burst to be from short (or type I) population with probability of $\sim 74\%$, estimated from duration distribution of SPI-ACS bursts (see Fig. 11 in Minaev & Pozanenko 2017).

We did not find any precursor or extended emission components in SPI-ACS data at time scales from 0.05 up to 100 seconds in time interval (-50, 200) s since GW trigger. We estimated upper limits on their intensity in both counts and energetic units using conversion factor described above. At time scale of 0.05 s upper limit on precursor activity is $S_{prec} \simeq 250$ counts or $S_{prec} \simeq 2.5 \times 10^{-8}$ erg/cm^2 at 3σ significance level. At time scale of 50 s upper limit on extended emission activity is $S_{EE} \simeq 8100$ counts or $S_{EE} \simeq 8.1 \times 10^{-7}$ erg/cm^2 at 3σ significance level.

Assuming redshift z = 0.009787 and luminosity distance $D_L = 42.5$ Mpc for the source (D'Elia et al. 2017) we estimated total isotropic energy release in energy range (75, 1000) keV as $E_{iso} = (3.9 \pm 0.9) * 10^{46}$ erg. One can estimate the upper limits on precursor and extended emission component expressed as total isotropic energy release as well: $E_{iso}^{prec} = 5.3 * 10^{45}$ erg and $E_{iso}^{EE} = 1.7 * 10^{47}$ erg, correspondingly.

3.2. *GBM/Fermi*

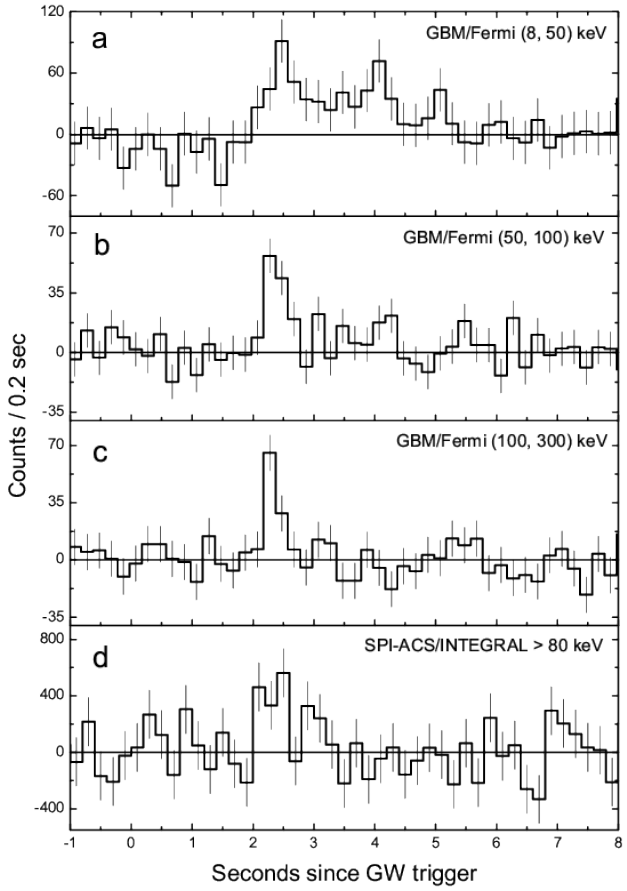

FIG. 4.— Background subtracted light curve of GRB 170817A in data of GBM/Fermi (NaI: 1, 2, 5) in (8, 50) keV (a), (50, 100) keV (b), (100, 300) keV (c) and in data of SPI-ACS/INTEGRAL (d). Time in seconds since GW trigger (UTC 2017-08-17 12:41:04) is on x-axis, counts over 0.2 s time bins on y-axis. Flux uncertainties are presented at 1σ significance level.

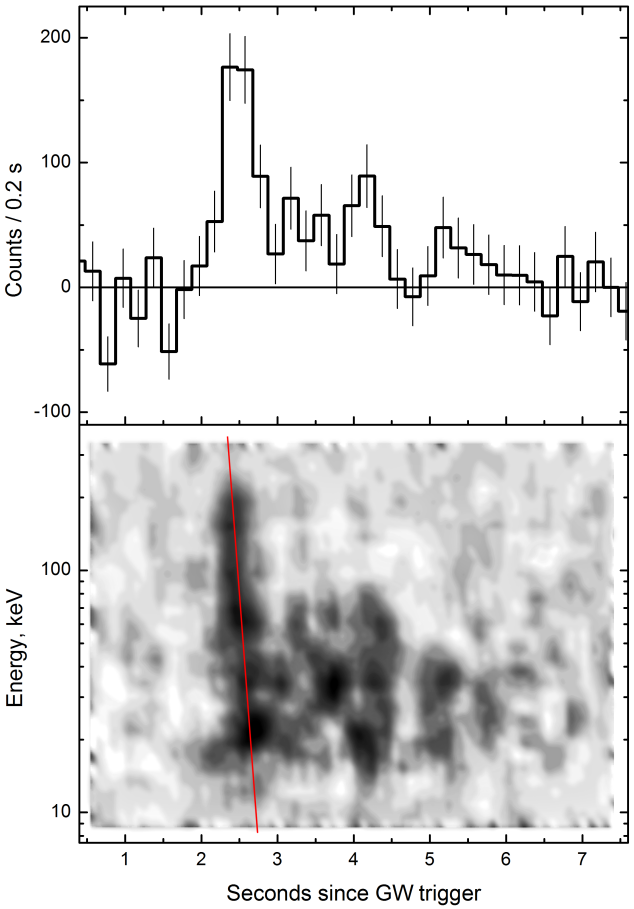

FIG. 5.— Background subtracted light curve of GRB 170817A in (8, 300) keV range (top) and energy diagram (bottom) in data of GBM/Fermi (NaI: 1, 2, 5). Time in seconds since GW trigger (UTC 2017-08-17 12:41:04) is on x-axis, counts over 0.2 s time bins for light curve and energy in units of keV for energy diagram are on y-axis. Flux uncertainties are presented at 1σ significance level at light curve. A darker shade on the diagram corresponds to a higher flux. Two component (pulse) structure of GRB 170817A is seen. For the first pulse red line represents logarithmic spectral lag behavior on energy, $lag \sim 0.24 \times log(E)$. The semi-logarithmic approximation is typical for single pulses of GRBs (Minaev et al. 2014).

We used the publicly accessible FTP archive (ftp://legacy.gsfc.nasa.gov/fermi/data/) as the source of the GBM/Fermi data.

GRB 170817A was detected in GBM/Fermi (NaI: 1, 2, 5) at 8.7σ significance level in (8, 300) keV energy range. Background subtracted light curve of the burst in GBM/Fermi data with time resolution of 0.2 s is presented in three energy channels on panels a, b, c at Figure 4. The burst onset in GBM/Fermi data is delayed to GW trigger to $\simeq 2$ s as well as in SPI-ACS data. Third order polynomial model was used to fit background signal in time intervals (-40, -5) and (20, 70) s for all presented GBM/Fermi light curves.

As seen at Figure 4, light curve of the burst consists of two different components (pulses): the first one is short hard, the second one is visible only in soft energy range (8, 50) keV. Two component structure of the burst is also confirmed by duration measurements: in (8, 70) keV energy range burst duration is $T_{90}^{8-70\ keV} = 2.9 \pm 0.3$ s, which is six times longer than duration in (70, 300) keV energy range, $T_{90}^{70-300\ keV} = 0.5 \pm 0.1$ s. The duration in (8, 300) keV range was found to be comparable with one in (8, 70) keV range, $T_{90}^{8-300\ keV} = 3.0 \pm 0.3$ s.

Light curve of GRB 170817A in (8, 300) keV range and energy diagram in data of GBM/Fermi (NaI: 1, 2, 5) are presented on Figure 5.

To construct and fit the energy spectra, we used the RMfit v4.3.2 software package specially developed to analyze the GBM data of the Fermi observatory (http://fermi.gsfc.nasa.gov/ssc/data/analysis/rmfit/). The method of spectral analysis is similar to that proposed by Gruber et al. (2014), who also used the RMfit software package. To fit the energy spectra and to choose an optimal spectral model, we used modified Cash statistics (CSTAT; see Cash 1979) instead of the χ^2 test.

Results of spectral analysis performed for GRB 170817A using data of GBM/Fermi (NaI: 1, 2, 5) are summarized in Table 3. We analyzed three time intervals, covering the whole burst (-0.5, 3.0) s since GBM trigger, the first hard pulse (-0.5, 0.25) s and the second soft pulse (0.25, 3.0) s with three spectral models: simple power law (PL), power law with exponential cutoff

TABLE 3
Results of spectral analysis of GRB 170817A based on GBM/Fermi data

Time interval [a] (s)	Model [b]	α	$E_{\rm peak}$ [c] (keV)	Fluence [d] (10^{-7} erg/cm^2)	Hardness ratio [e]	CSTAT/dof
(-0.5, 0.25)	PL	-1.4 ± 0.1	-	3.3 ± 0.5	0.9 ± 0.2	406/345
first	BB	-	35 ± 5	1.5 ± 0.2	3.3 ± 0.9	413/345
pulse	CPL $\star$	$-0.8^{+0.4}_{-0.3}$	270^{+und}_{-100}	2.6 ± 0.7	1.2 ± 0.3	401/344
(0.25, 3.0)	PL	-1.9 ± 0.2	-	2.0 ± 0.6	0.4 ± 0.1	365/255
second	BB $\star$	-	11.0 ± 1.4	1.1 ± 0.2	0.23 ± 0.08	356/255
pulse	CPL	$1.2^{+2.0}_{-1.7}$	$42.8^{+6.3}_{-5.4}$	1.1 ± 0.2	0.23 ± 0.10	356/254
(-0.5, 3.0)	PL	-1.6 ± 0.1	-	5.1 ± 0.9	0.59 ± 0.12	384/255
whole	BB	-	14.2 ± 1.3	1.9 ± 0.2	0.47 ± 0.11	389/255
burst	CPL $\star$	$-1.3^{+0.9}_{-0.4}$	129^{+und}_{-64}	3.3 ± 0.9	0.60 ± 0.13	382/254

[a] – time interval relative to GBM trigger (UTC 2017-08-17 12:41:06.475).
[b] – PL is for power law, CPL is for power law with an exponential cutoff, BB for a thermal model.
[c] – for the BB spectral model the $E_{\rm peak}$ column gives the parameter kT.
[d] – fluence in (10, 1000) keV energy range.
[e] – hardness ratio calculated as ratio of photon fluxes in (50, 300) keV and (15, 50) keV energy bands.
$\star$ – optimal spectral model.

(CPL) and thermal model (BB).

The energetic spectrum of whole burst (time interval (-0.5, 3.0) s) is best fitted by CPL model with $\alpha = -1.3^{+0.9}_{-0.4}$ and $E_{\rm peak} = 129^{+und}_{-64}$ keV (the $+1\sigma$ error is beyond GBM(NaI) energy range (8, 900) keV). The fluence in (10, 1000) keV range is F = $(3.3 \pm 0.9) \times 10^{-7}$ erg/cm^2. Using CPL spectral model we calculated hardness ratio of photon fluxes between (50, 300) keV and (15, 50) keV energy bands, HR = 0.60 ± 0.13. Hardness ratio of HR = 0.60 ± 0.13 along with duration $T_{90}^{70-300\ keV} = 0.5 \pm 0.1$ s characterizes the burst to be typical short but soft one (e.g., see Fig. 6 in von Kienlin et al. 2014). The probability of GRB 170817A to be from short population was estimated using duration and hardness values in Goldstein et al. (2017) and found to be $P \simeq 73\%$.

The optimal spectral model for the first pulse (time interval (-0.5, 0.25) s) of the GRB 170817A is CPL model (Table 3) with $\alpha = -0.8^{+0.4}_{-0.3}$ and $E_{\rm peak} = 270^{+und}_{-100}$ keV (the $+1\sigma$ error is beyond GBM(NaI) energy range (8, 900) keV). Using CPL spectral model we calculated hardness ratio between (50, 300) keV and (15, 50) keV energy bands, HR = 1.2 ± 0.3, which describes the first pulse as hard one (see Fig. 6 in von Kienlin et al. 2014).

The optimal spectral model for the second pulse (time interval (0.25, 3.0) s) of the GRB 170817A is thermal model with kT = 11.0 ± 1.4 keV and fluence in (10, 1000) keV energy range F = $(1.1 \pm 0.2) \times 10^{-7}$ erg/cm^2 (Table 3). CPL model gives the same goodness of fit, but with positive value of $\alpha = 1.2^{+2.0}_{-1.7}$. The $E_{\rm peak}$ parameter was found to be $E_{\rm peak} = 42.8^{+6.3}_{-5.4}$ keV within CPL model. The hardness ratio between (50, 300) keV and (15, 50) keV energy bands within CPL model, HR = 0.23 ± 0.10, which describes the second pulse to be very soft one (see Fig. 6 in von Kienlin et al. (2014)).

We did not find any precursor or extended emission components in GBM/Fermi data at time scales from 0.1 up to 20 seconds in the time interval (-10, 30) s since GBM trigger. To estimate upper limits on their intensity in energetic units we derived conversion factor in (8, 300) keV range using count fluence of the burst and energetic fluence within CPL spectral model (Table 3). We found that 1 count in GBM/Fermi corresponds to $\sim 3.2 \times 10^{-10}$ erg/cm^2 in energy range (8, 300) keV. At time scale of 0.1 s upper limit on precursor activity is $S_{prec} \simeq 1.6 \times 10^{-8}$ erg/cm^2 at 3σ significance level. At time scale of 20 s upper limit on extended emission activity is $S_{EE} \simeq 2.3 \times 10^{-7}$ erg/cm^2 at 3σ significance level.

Spectral lag analysis based on CCF method (see e.g. Minaev et al. 2014) was performed for GRB 170817A using GBM/Fermi (NaI: 1, 2, 5) data between light curves, constructed in energy channels (8, 50) keV, (50, 100) keV and (100, 300) keV with time resolution of 0.04 s. Spectral lag between (8, 50) keV and (50, 100) keV bands is negligible, lag = 0.01 ± 0.08 s, but between (8, 50) keV and (100, 300) keV lag is quiet positive, lag = 0.27 ± 0.05 s. Most probably it represents the spectral evolution of the first pulse (see Figure 4). We also obtained time lag between SPI-ACS and GBM light curve in (100, 300) keV range, which characterizes mostly the difference in light traveling time from the source to INTEGRAL and Fermi observatories. It was found to be lag = 0.09 ± 0.12 s.

3.3. *Amati relation*

One of the interesting phenomenological relations for GRBs is Amati diagram, i.e., the dependence of the equivalent isotropic energy $E_{\rm iso}$ emitted in the gamma-ray range (1, 10000) keV on parameter $E_{\rm peak}(1+z)$ in the source frame (Amati 2010). Long bursts obey well this law, while short bursts usually lie on the diagram above the main correlation region of long bursts (at the same value of $E_{\rm iso}$ for short bursts $E_{\rm peak}(1+z)$ is considerably higher). Thus, Amati diagram can also be used for the classification of GRBs.

Using the the experimental data given in (Volnova et al. 2014; Svinkin et al. 2016; Qin & Chen 2013) we constructed the Amati diagram for 134 long and 20 short bursts and fitted the relation for both types of bursts with power-law like logarithmic model: $\log\left(\frac{E_{\rm peak}(1+z)}{1{\rm keV}}\right) = K \log\left(\frac{E_{\rm iso}}{1erg}\right) + B$. We derived $K_{\rm short} = 0.50 \pm 0.04$ and $B_{\rm short} = -22.4 \pm 1.8$ with $\chi^2/dof = 499/18$ for short bursts, $K_{\rm long} = 0.46 \pm 0.02$ and $B_{\rm long} = -21.8 \pm 1.0$ with $\chi^2/dof = 5038/132$ for long ones (dotted lines at Figure 6). One can emphasize the same index $K \simeq 1/2$ for both burst classes within 1σ

TABLE 4
GRB 170817A ENERGETICS

Time interval [a] (s)	Spectral model [b]	Flux [c] 10^{-7} erg/(cm$^2 s$)	Fluence [d] 10^{-7} erg/cm^2	$E_{\rm iso}$ 10^{46} erg	$L_{\rm iso}$ 10^{46} erg/s
(-0.5, 0.25)	CPL	3.5 ± 1.2	2.6 ± 0.9	5.6 ± 1.9	7.5 ± 2.6
(0.25, 3.0)	BB	0.40 ± 0.06	1.1 ± 0.2	2.4 ± 0.4	0.86 ± 0.13
(-0.5, 3.0)	CPL	1.0 ± 0.3	3.5 ± 1.0	7.5 ± 2.1	2.1 ± 0.6

[a] – relative to GBM trigger (UTC 2017-08-17 12:41:06.475).
[b] – CPL is for power law with an exponential cutoff, BB for a thermal model.
[c] – energy flux in (1, 10000) keV energy range.
[d] – energy fluence in (1, 10000) keV energy range.

uncertainties. The high value of χ^2/dof for both samples is connected with relatively low degree of correlation due to various effects (e.g. intrinsic differences of bursts or some systematics at spectrum modeling stage including usage of data from different experiments).

To estimate uncertainties for power-law fits we used not only statistical ones based on the χ^2 approximation method, but also investigated selection effects of the samples, which are supposed to be quiet significant for short bursts. As seen in Figure 6, there are two short bursts with small uncertainties in $E_{\rm iso}$ and $E_{\rm peak}(1+z)$ at the bottom left and top right of the diagram, which give very significant influence at power-law fit. In case of long bursts there are four bursts (two at bottom left and two at top right) with similar behavior. To estimate selection effects we formed several subsamples of bursts, consisted of all bursts from the total sample except the one or two brightest (faintest) ones for both short and long burst samples, and then fitted the relation for the subsamples. Dashed lines on Figure 6 bound the 2σ region of fits including selection effects. It is clear from the figure that selection effects are huge for short bursts as expected and not so significant for long ones.

Using optimal spectral models derived in previous subsection for GRB 170817A and its two pulses (Table 3) we estimated $E_{\rm iso}$, $L_{\rm iso}$ parameters in (1, 10000) keV range (Table 4). All of three components lie far above the 2σ correlation region for both short and long bursts (Figure 6). The burst itself is the faintest one ever registered with known redshift. If we assume that the burst GRB170817A should obey Amati relation we can draw a trajectory of the burst parameters as $E_p \sim E_{\rm iso}^{1/3}$ if it is a cone relativistic jet emission, and $E_p \sim E_{\rm iso}^{1/4}$ if it is a spherical relativistic emission. One can see that neither trajectories cross the Amati relation at reasonable $E_{\rm iso}$. It requires alternative explanation for the nature of the first hard pulse.

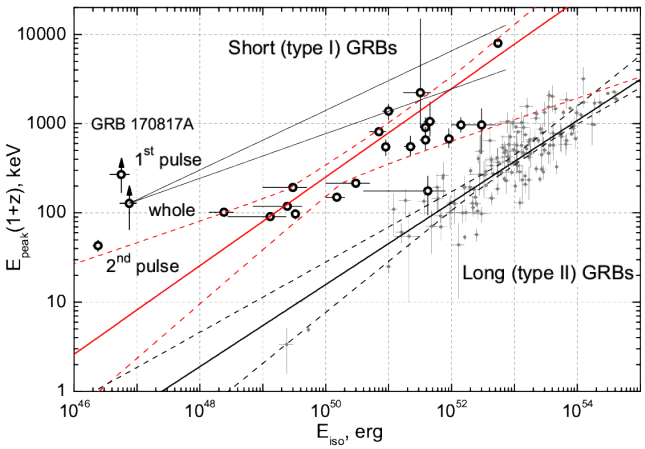

FIG. 6.— Amati diagram, the dependence of the equivalent isotropic energy $E_{\rm iso}$ emitted in the (1, 10000) keV range on $E_{\rm peak}(1+z)$ in the source frame (Amati 2010). The diagram was constructed for long (filled gray circles) and short (open circles) bursts. Black (red) solid straight line indicates a power-law fit to the dependence for long (short) bursts; dashed lines bound the 2σ region for power-law fits including selection effects. Black lines starting from point for the whole GRB 170817A indicate the dependence $E_{\rm peak}(1+z) \sim E_{\rm iso}^{1/3}$ and $E_{\rm peak}(1+z) \sim E_{\rm iso}^{1/4}$. Uncertainties for $E_{\rm iso}$ and $E_{\rm peak}(1+z)$ are presented at 1σ significance level.

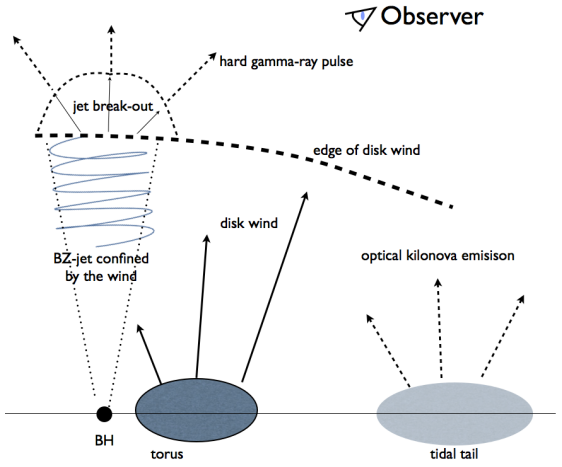

FIG. 7.— The sketch of our scenario. After merging of NSs a BH is formed, which is surrounded by compact accretion disk with intensive wind. After sufficient magnetic flux is accumulated on the BH an electromagnetic jet is launched, confined initially by the disk wind. After propagating with mildly relativistic velocities the jet breaks out from the wind zone in a semi-isotropic fashion, reaching highly relativistic Lorentz factors. This is the prompt GRB.

4. THE SCENARIO

4.1. *Overall description*

The key points of the model are illustrated in Figs. 7-8.

The detection of the EM signal contemporaneous with gravitational waves is consistent with the binary NS scenario for short GRB (Blinnikov et al. 1984; Paczynski 1986a; Eichler et al. 1989a). Qualitatively, the evolution of merging neutron stars follows a well-defined path (*e.g.* Ruiz et al. 2016; Radice et al. 2016; Baiotti & Rezzolla 2017, and many others), though many details, like the effects of different equations of states, various mass ratios,

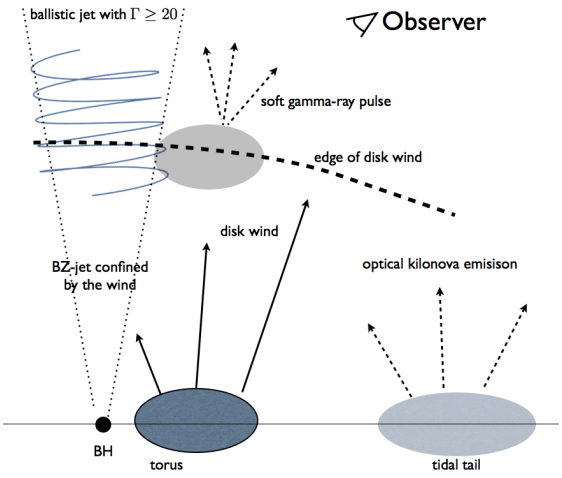

FIG. 8.— Post-break out structure of the flow. The wind from the disk keeps collimating the jet for a few seconds. Jet propagates ballistically with Lorentz factors ≥ 20 and is unobservable due to deboosting. The shocked wind material produces thermal extended γ-ray component with $T \sim 10$ keV.

initial spins and magnetic field evolution, remain to be settled. An active stage of a merger lasts $\sim 10-100$ milliseconds after which the neutron stars collapse into BH. [3] The BH is fairly fast rotating with the Kerr parameter $a \sim 0.5$. The mass of the resulting BH is somewhat smaller than the sum of masses due to emission of neutrinos, gravitational waves and ejection of the material. The amount of the ejected material is especially uncertain, but is of utmost importance for the production of the EM signal. It is expected that, first, tidal tails eject $0.01M_\odot$ with outflow speed $v_{\rm ex} \approx 0.1-0.3$ c. This material is likely a sight of r-element production and can be seen as a kilonova – an optical emission of peak luminosity $\sim 10^{41}$ erg s $^{-1}$ lasting for few weeks.

Second, during the merger an accretion torus of $\sim 0.01M_\odot$ forms around the BH with viscous time 0.1 s (Ruiz et al. 2016; Radice et al. 2016; Baiotti & Rezzolla 2017). Highly different masses of merging NS are good for formation of massive disk, and hence jet power and its confinement. This accretion disk plays the most important part in our model. For a few seconds the disk undergoes viscose spreading, produces powerful neutrino-driven winds and exercise accretion onto the BH via the inner edge (presumably close to the innermost stable orbit), see §6.1. Interesting, that in the case of BH-NS merging the neutrino heating mechanism (Eichler et al. 1989b; Birkl et al. 2007; Zalamea & Beloborodov 2011) can be the main source of jet's energy (see Barkov & Pozanenko 2011). In the case of NS+NS merging the mass of the accretion torus is relatively small ($< 10^{-2}M_\odot$), so neutino heating mechanism can not be efficient on time scales of a few seconds.

At the same time, magnetic fields are amplified within the disk to $\sim 10^{15}$ G (Rezzolla et al. 2011) due to the development of MRI and the presence of the velocity shear. As the matter is accreted onto the BH, the BH accumulates magnetic flux. Accumulation of the magnetic flux leads to a delay for the jet's switch-on. At the same time baryons slide off into the BH along magnetic field lines, leaving polar regions with low density. This creates conditions favorable for the operation of the Blandford-Znajek (BZ) mechanism (Blandford & Znajek 1977; Komissarov & Barkov 2009).

The BZ mechanism - production of EM outflows from the magnetic field supplied by the disk - also requires the presence of the external medium to produce jets (collimated outflows). It is the heavy baryonic wind from the disk that provides the required collimating surrounding, §6.2. Importantly, the disk wind has only limited spacial extent - propagating with velocity of ~ 0.1 for about a few seconds it reaches out only to few $\times 10^9$ cm. Outside of the wind the surrounding is very clean.

The BZ jet propagates through a dense wind with mildly relativistic velocity, §6.4. At the same time the jet is mildly dissipative, §6.5 (and thus highly optically thick). In few seconds the head of the EM jet reaches the edge of the wind. During the break-out the head part of the jet expands with highly relativistic velocities both long the jet propagation and the sideway. Sudden expansion leads to pair annihilation and the production of gamma-ray emission in a manner similar to conventional models of GRBs, §6.5. This is the prompt GRB.

After the jet break-out from the wind, a rarefaction wave propagating towards the BH leads to the acceleration of the jet, that looses internal causal contact and propagates nearly ballistically, Fig. 8. Since the jet emission is highly de-beamed, the jet becomes unobservable. The wind emission shocked by the breaking-out jet produces the soft tail, Fig. 8.

5. OUTFLOW PARAMETERS INFERRED FROM OBSERVATIONAL CONSTRAINTS

5.1. *Lorentz factor for the prompt spike*

For the hard prompt emission, using the total fluence of 2.6×10^{-7}erg cm^{-2}, the total energetics estimates to $\sim 5.6 \times 10^{46}$ erg, with peak power $\sim 10^{47}$ erg s^{-1}. The corresponding compactness parameter is large

$$l_c = \frac{L_\gamma \sigma_T}{m_e c^4 t} = 3 \times 10^8 t_{-0.3}^{-1} \qquad (1)$$

Since the optical depth to pair production is $\propto l_c/\Gamma^6$ (*e.g.* Goodman 1986; Lithwick & Sari 2001), it is required that the flow producing the prompt burst accelerates to

$$\Gamma_{\rm j,min} = \left(\frac{\sigma_{\rm T} L_{\rm ht}}{m_{\rm e} c^4 t}\right)^{1/6} \approx 25. \qquad (2)$$

This in turn requires the emitting jet to be sufficiently clean (lacks baryons). This is an important constraint since the neutron-rich environment is expected to pollute the jet (Derishev et al. 1999; Beloborodov 2003).

5.2. *Opening angle of the jet from soft γ-ray component*

Properties of the soft thermal emission can be used to infer the geometrical properties of the outflow. (In our model the soft γ-ray component originates from the wind material shocked by the jet and thus should have physical size of the order of the jet radius at the moment

[3] We disfavor alternative scenarios, like the formation of a supermassive fast rotating neutron star with strong magnetic field (Bisnovatyi-Kogan 1970; LeBlanc & Wilson 1970; Usov 1992; Metzger et al. 2008b) as they require existence of very massive neutron stars.

of break-out.) Total (thermal) luminosity of the second soft component is $L_{\rm ee} = 0.9 \times 10^{46}$ erg/s. Thus, the emitting area is

$$S = \frac{L_{\rm ee}}{\sigma_{SB} T_{\rm ee}^4} = 1.1 \times 10^{18} {\rm cm}^2 \quad (3)$$

and the radius of emitting region is

$$r_{\rm S} = \sqrt{\frac{S}{\pi}} = 6 \times 10^8 {\rm cm} \quad (4)$$

If the wind from the torus propagates with velocity $v_{\rm ex} =$ 0.1 c, then in 2.4 sec it would expand to $r_w = 7 \times 10^9$ cm. Thus, the jet opening angle is

$$\theta_{\rm j} = \frac{r_{\rm S}}{r_w} = 0.08. \quad (5)$$

This value agrees well with GRMHD simulations of (Barkov 2008; Barkov & Baushev 2011; Kathirgamaraju et al. 2017).

5.3. *Magnetic field at the source*

As the jet breaks out from the wind, the quasi-spherical expansion of the jet material will form a fireball that resembles a pair-loaded fireball discussed earlier in the literature (Paczynski 1990; Rees & Mszros 2005). A fraction $\eta_{\rm em} \ll 1$ of the energy stored in the pre-break out wind will be radiated ($\eta_{\rm em}$ depends on parameters of outflow like the energy injection rate, magnetization, and baryonic loading, (*e.g.* Lyutikov & Usov 2000).

We can relate the observed flux in the first/hard peak to the jet had energy density as

$$u_{\rm em} = \eta_{\rm em} \frac{4 L_{\rm peak}}{Sc} \quad (6)$$

This can be used to estimate the equipartition magnetic field B_{eq} in the jet (this will give a lower limit on the field in jet):

$$B_{\rm eq} = \frac{\sqrt{8\pi u_{\rm em}}}{\sqrt{3}} \approx 3 \times 10^{10} \eta_{\rm em,1}^{1/2} \ {\rm G} \quad (7)$$

If originating from a BH with the surface field B_{BH}, the magnetic field at the emission cite is

$$B_{\rm eq} = B_{BH} \left(\frac{r_{\rm g}}{R_{\rm LC}} \right)^2 \frac{R_{\rm LC}}{r_{\rm S}} \quad (8)$$

where $R_{LC} \sim 4 r_{\rm g}/a$ is the light cylinder radius, a is the Kerr parameter. (Scaling is different from the NS case, here it's R_{LC}^2 not R_{LC}^4.)

Thus, the magnetic field on the BH can be estimated as

$$B_{BH} > \frac{4}{a} \frac{r_{\rm S}}{r_{\rm g}} B_{\rm eq} \sim 3 \times 10^{14} \eta_{\rm em,1}^{1/2} a_{-0.3}^{-1} \ {\rm G} \quad (9)$$

where we scaled the Kerr parameter to 0.5. These fields are higher, by about one or two orders of magnitude that is expected from surface magnetic fields on merging neutron stars, indicating that a dynamo process was operational during/or after the merger (either on the collapsing neutron star or in the surrounding torus).

The expected power of the jet is then

$$L_j > 7 \eta_{\rm em} L_{\rm peak} \sim 10^{49} \eta_{\rm em,1} \ {\rm erg \ s^{-1}} \quad (10)$$

(To reiterate, Eq. (10) related the power $L_{\rm ee}$ of the hard γ-ray emission to the power of the BZ jet L_j.) The estimate (10) compares favorably to the estimate of the jet power derived from modeling the evolution of the accretion torus, Eq. (16) and conversion parameter $\eta_{\rm em} \approx 10$ which is corresponds jet power on the level 10^{49} erg s^{-1} (see Paczynski 1990).

6. THE MODEL

6.1. *Evolution of the accretion disk*

As the matter is accreted from the torus onto the BH, the magnetic flux is accumulated on the BH. This triggers the BZ mechanism. It is expected that the value of the magnetic field that can be accumulated on the BH, and thus the jet power, depend on the accretion rate. Let us next estimate the the maximal luminosity of a magnetically driven jet.

The accretion rate from the disc is $\dot{M}_d = 1.6 M_{\rm d}/t_{\rm vis}$ (Shakura & Sunyaev 1973; Metzger et al. 2008a). Wind from disc surface can significantly reduce accretion rate at the inner parts of the disk. Using model Blandford & Begelman (1999) and following Metzger et al. (2008a), the accretion rate to the BH can be calculated as:

$$\frac{dM_{\rm BH}}{dt} = \frac{dM_{\rm d}}{dt} \left(\frac{r_{\rm ISCO}}{r_{\rm d}} \right)^{-p}. \quad (11)$$

here $0 < p < 1$ is non-dimensional parameter which describe wind intensity,

$$r_{\rm d} = \left(\alpha_{\rm ss}^2 h_{\rm d}^4 G M_{\rm BH} t^2 \right)^{1/3}, \quad (12)$$

here $h_{\rm d} = H/R$ is relative thickness of the disk and $\alpha_{\rm ss}$ is non-dimensional viscose parameter. The radius of the innermost stable circular orbit (ISCO) is

$$r_{\rm ISCO} = \frac{G M_{\rm BH} f(a_{\rm BH})}{c^2}, \quad (13)$$

here $1 < f(a_{\rm BH}) < 6$ is unidimensional radius of last marginally stable orbit (Bardeen et al. 1972) which is function of BH spin parameter "$a_{\rm BH}$".

The accretion rate to BH is

$$\frac{dM_{\rm BH}}{dt} = \frac{0.16 (2p+1)^{\frac{4(p+1)}{3}} f(a_{\rm BH})^p M_{\rm d,-2} M_{\rm BH,0.5}^{\frac{2p}{3}} t_{\rm vis,-1}^{\frac{(2p+1)}{3}}}{60^p h_{\rm d,-0.5}^{\frac{4p}{3}} \alpha_{\rm ss,-1}^{\frac{2p}{3}} ((2p+1) t_{\rm vis,-1} + 48t)^{\frac{4(p+1)}{3}}} \quad M_\odot \ {\rm s^{-1}}. \quad (14)$$

If we assume conservative value $p = 1/2$ the Eq. (14) takes form

$$\frac{dM_{\rm BH}}{dt} = 0.02 \frac{f(a_{\rm BH})^{1/2} M_{\rm d,-2} M_{\rm BH,0.5}^{1/3} t_{\rm vis,-1}^{2/3}}{h_{\rm d,-0.5}^{2/3} \alpha_{\rm ss,-1}^{1/3} (t_{\rm vis,-1} + 24t)^2} \quad M_\odot \ {\rm s^{-1}}. \quad (15)$$

The maximal jet power can be $L_{\rm BZ} = C(a_{\rm BH}) \dot{M}_{\rm BH} c^2$, here $0 < C(a_{\rm BH}) <$ few efficiency of accretion coefficient (see eg. Komissarov & Barkov 2010; McKinney et al. 2012), which can be combined with factor $f(a_{\rm BH})$ and we get for wide range of BH spin parameter $C(a_{\rm BH}) f(a_{\rm BH})^{1/2} \sim 0.3$.

$$L_{\rm BZ} \sim 10^{49} M_{\rm d,-2} M_{\rm BH,0.5}^{1/3} t_{\rm vis,-1}^{2/3} t_{0.3}^{-2} \quad {\rm erg \ s^{-1}}. \quad (16)$$

Such electromagnetic luminosity corresponds to strength of magnetic field near horizon order of (Blandford & Znajek 1977; Barkov & Komissarov 2008b)

$$B_{\rm BH} \approx \left(\frac{24 L_{\rm BZ}}{r_{\rm g}^2 c}\right)^{1/2} \sim 2\times 10^{14} \quad {\rm G}. \tag{17}$$

This fields, inferred from modeling the accretion torus, compare well with the one inferred from the soft X-ray component, Eq. (9)

6.2. *Jet confinement by the disk wind*

Next we discuss the jet confinement by disk wind. The question we would like to answer is "Can the wind from the torus provide the jet confinement?".

The properties of the disk evolve quickly, on viscose time scale of ≤ 1 sec, so they change considerably during the observations. The confinement of the jet depends both on the jet power (that provides an outward-directed forces) and the wind luminosity (that provides confining forces). Both of these depend on the properties of the disk (*e.g.*, higher accretion rate, higher jet power, but also more powerful winds). Thus, we expect that confinement properties change less than, *e.g.* the relative change of the accretion rate.

Let us use parameters for the disk wind appropriate at later times, during the soft phase. Let's assume the disk provides an outflow

$$\dot{M}_{\rm w,disk} = 4\pi v_w \rho_w r^2. \tag{18}$$

In order to confine the jet the momentum flux in the wind should be higher than the pressure created by the jet (since both the wind and the jet are moving away from the BH). In §5.2 we related the energy density in the jet to the energy density of soft X-ray photons. Thus

$$\eta_w \rho_w v_w^2 = u_{em} \tag{19}$$

where $\eta_w < 1$ accounts for mismatch between the wind ram pressure and the jet pressure. This requires

$$\dot{M}_{\rm w,disk} = 4\pi \frac{u_{em} r^2}{v_w \eta_w} = 16\pi \frac{v_w \tau^2 \sigma_{SB} T_{\rm ee}^4}{c\eta_w} = 10^{-3} M_\odot \ {\rm s}^{-1} \tag{20}$$

for $\eta_w = 0.1$. This is a reasonable estimate for the wind mass loss at times of few seconds. Since at that time the disk mass is expected to be $M_d \sim$ few 10^{-3}, the wind will be powered for a few seconds. We conclude that the disk wind can provide the collimation of the BZ jet with the required powers.

6.3. *Optically thick pair-loaded wind from the disk*

The wind originates in a very hot disk with $T \sim 1$ MeV. The wind is very optically thick even without pair creation the expected optical depth to Thomson scattering is $\tau_T \gg 1$,

$$\tau_T \approx \frac{3\sigma_T M_{\rm d}}{4\pi m_p v_{\rm ex}^2 t^2} \sim 5\times 10^{10} M_{\rm d,-2} v_{\rm ex,-1}^{-2} t_{0.3}^{-2}. \tag{21}$$

As a result large number of electron-positron pairs will be created. But the $e^\pm$ pairs do not affect wind dynamics since baryon density exceeds the pair density by many orders of magnitude,

$$\frac{\rho_w}{m_e n_\pm} = \frac{\sqrt{\pi/2}}{4} \frac{e^{r/(r_0\theta_{T,0})}}{m_e v_w r^{1/2} r_0^{3/2} \theta_{T,0}^{3/2}} \gg 1$$
$$n_\pm \lambda_C^3 = \frac{\sqrt{2}}{\pi^{3/2}} e^{-\frac{1}{\theta_T}} \theta_T^{3/2} \tag{22}$$

where $\lambda_C = \hbar/(m_e c)$ is the electron Compton length and we assumed the wind temperature is $T = T_0(r_0/r)$, scaled $T = m_e c^2 \theta_T$ (and similar for T_0) and used the equilibrium thermal pair density $n_\pm$ (Lightman 1982; Svensson 1982).

If the wind just cools adiabatically, it won't produce any appreciable EM signatures from the wind due to steep adiabatic cooling. It is expected that radiative elements decay contributes to wind heating, which together with far-flung tidal tails produce the kilonova emission (Li & Paczyński 1998; Metzger et al. 2010).

6.4. *Jet propagation within the wind*

Next we consider the propagation of the BZ jet through the disk-generated wind. Since it takes time to accumulate the magnetic flux on the BH and to trigger the BZ mechanism, the jet will propagate through the pre-existing wind. Let the wind have constant properties (we neglect the fact that at early times the wind has higher $\dot{M}$; we might expect that this will be partially compensated by the initially higher v_w.) Consider a jet of power L_j that is confined within a solid angle $4\pi\Delta\Omega$. The head of the jet located at r_h propagates according to (in the Kompaneets approximation, Kompaneets 1960)

$$P_{\rm jh} = \frac{L_j}{\pi\theta^2 r_h^2 c} = \rho_w (\partial_t r_h - v_w)^2. \tag{23}$$

where $P_{\rm jh}$ is the pressure created by the jet. Using wind density from (18), the jet head propagates according to

$$r_h = r_0 + \left(v_w + \sqrt{\frac{4Lv_w}{\theta^2 \dot{M}_{\rm w,disk} c}}\right) t$$
$$v_{\rm jh} = v_w + \sqrt{\frac{4Lv_w}{\theta^2 \dot{M}_{\rm w,disk} c}} = v_w + 5\times 10^9 {\rm cm\ s}^{-1} \tag{24}$$

where $r_0 \sim 10^7$ cm is the initial radius.

Thus, the jet propagates with nearly constant velocity. The jet propagation time is

$$t_{\rm jb} = \frac{v_{\rm ex} t}{v_{\rm jh}} \sim \frac{t_{\rm delay}}{3}. \tag{25}$$

This delay time is in a good agreement with results of statistical analysis of short GRBs Moharana & Piran (2017). Importantly, the head propagates within the wind with non-relativistic velocity.

The speed of jets head shock $v_{\rm s} = v_{\rm jh} - v_w$, should be larger than the wind speed to avoid formation too spherical cocoon. So, comparing $v_{\rm s}$ and v_w, from Eqs (24) and (5) we can derive restriction on the jet power as

$$L_{\rm j} \geq \frac{S\dot{M}_{\rm w,disk} c}{4\pi v_w t_{\rm delay}^2} \sim 3\times 10^{48} \dot{M}_{\rm w,disk,-2} v_{w,-1}^{-1} \ {\rm erg\ s}^{-1}. \tag{26}$$

6.5. *Jet break-out – prompt hard GRB*

The BZ mechanism of jet launching requires clean plasma – there should be little mass loading and magnetic dissipation close to the source. This is indeed expected if the flow originates on field lines that penetrate the BH. It is expected that a jet launched by the BH is highly magnetized, $\sigma \gg 1$. Importantly, the confined jet with $\sigma \gg 1$ that propagates with non-relativistic velocity must necessarily be dissipative (Lyutikov 2006). Briefly, the magnetic flux and energy are supplied to the inflating bubble by a rate that cannot be accommodated within the bubble (this problem is also known as the σ-problem in pulsar winds Rees & Gunn 1974; Kennel & Coroniti 1984). If a dissipation becomes important that will destroy a significant fraction of the magnetic energy and most importantly the toroidal flux will be eliminated. Latest 3D numerical simulations of pulsar wind nebula indeed demonstrate that magnetic flux (and some magnetic energy) are dissipated within non-relativistically expanding cavities, thus resolving the sigma-problem (Porth et al. 2013, 2014). A considerable fraction of the magnetic energy that has been produced before the jet break-out is dissipated.

At the time of the jet break out it's magnetization is not very high. At the break-out the highly over-pressured jet lose both radial and lateral confinement. At this point the jet dynamics changes in two important ways. First the leading part of the jet expands nearly spherically, within a solid angle $\sim 2\pi$, with large Lorentz factors (see Lyutikov 2010; Lyutikov & Hadden 2012, for discussion of break-out dynamics in relativistic magnetized outflows; also, in Appendix B we construct a simple model of a break-out of magnetically dominated jet – the "force-free magnetic bomb"); the dynamics of non-magnetized relativistic break out flows was considered by Johnson & McKee (1971); Nakar & Sari (2012); for discussion of break-out dynamics in core collapse supernovae see, *e.g.*, Weaver (1976); Tan et al. (2001); Ensman & Burrows (1992). At this point the dynamics of pair-loaded magnetized outflows will resemble the conventional picture of magnetized GRB outflows (see, *e.g.* early discussion by (Lyutikov & Usov 2000); also Beloborodov (2017)).

We suggest that this nearly spherical, highly relativistic outflow produces the prompt GRB spike. As the optically thick jet breaks out from the confining disk wind the pair density falls out of equilibrium. Comptonization with the mildly optically thick region produces the observed GRB emission, similar to the photospheric emission in conventional GRB outflow (Beloborodov 2010; Beloborodov & Mészáros 2017). The emission is expected to peak at energies $\sim \Gamma\epsilon_{ph} \geq 400$ keV, where $\epsilon_{ph} \sim 20$ keV is the photospheric temperature in relativistic outflows Paczynski (1986b) and $\Gamma \geq 25$ is the bulk Lorentz factor, see Eq. (1).

Second, the bulk of the jet accelerates along the jet axis – there is no more wind material to plow through. As the bulk of the jet accelerates to $\Gamma \gg 1$ (see (1)), its propagation becomes nearly ballistic.

To estimate the energy of the prompt emission, we note that during break-out only a volume of the jet close to the surface contributes to quasi-spherical expansion - parts of the jet deep-in are accelerated during the passage of the rarefaction wave and produce a highly beamed-away outflow. Thus, the energy of the prompt emission can be estimated as

$$E_\gamma \sim \frac{4 r_{\rm S} L_{\rm BZ}}{\eta_{\rm em} c} \sim 2\times 10^{47} \eta_{\rm em,1}^{-1} L_{\rm BZ,49} \text{ ergs}. \qquad (27)$$

For $L_j \sim 10^{49}$ erg s^{-1}, and accounting for efficiency factor of converting jet power into radiation, the estimate (27) compares favorably with observations, Table 3.

6.6. *Post break-out jet acceleration*

Let's estimate the Lorentz factor of the magnetically driven jet after the break out from the wind. Magnetically driven jet can be accelerated up to very high Lorentz factor in linear regime (Beskin & Nokhrina 2006; Barkov & Komissarov 2008a; Komissarov et al. 2009). In the case of parabolic shape of the jet we can estimate the jet Lorentz factor on the border expanding envelop as $\Gamma_{\rm j} = (R_{\rm env}/r_{\rm lc})^{1/2}$, here envelop radius $R_{\rm env} = v_{\rm ex} t \approx 6\times 10^9$ cm and light cylinder radius $r_{\rm lc}$. In a case of fast spinning BH $r_{\rm lc} = 4 r_{\rm g} \approx 2\times 10^6$ cm, that corresponds $\Gamma_{\rm j,max} \approx 60 \beta_{\rm ex,-0.1}^{1/2} t_{0.3}^{1/2}$, here $\beta_{\rm ex,-1} = v_{\rm ex}/0.1c$. Several factors can reduce Lorentz factor of the jet: (i) high baryonic loading from neutron reach disc outflow; (ii) shape of jet's walls can significantly deviate from parabolic one; (iii) Distribution of energy flux and Lorentz factor versus off-axis angle are different and for large viewing angles the central parts of the jet (with smaller Lorentz factor) appears more brighter (see fig. 24 in Komissarov et al. 2009). Taking into account all these factors, we will adopt Lorentz factor of the jet $\Gamma_{\rm j} \approx 30$.

6.7. *The second thermal peak*

We can estimate the properties of the shock-heated wind flow at the point of break-out. Before the break-out the BZ jet drives a shock in the wind. This shock is strongly radiation-dominated, as we demonstrate next (see Katz et al. 2010, for discussion of radiation-dominated shocks). Equating post-shock plasma energy density to that of radiation, a shock becomes radiation-dominated for the post-shock (ion) temperatures T_r that satisfies

$$T_r > \left(\frac{60}{\pi}\right)^{1/3} c\hbar n^{1/3} \qquad (28)$$

where n is the pre-shock number density. The required shock velocity is then

$$v_r \geq 4\sqrt{\frac{\hbar}{m_p c}} n^{1/6} \qquad (29)$$

Comparing this with the relative velocity of the jet head with respect to the wind, (24),

$$\frac{v_{\rm jh} - v_w}{v_r} = \frac{\pi^{1/6}}{2^{2/3}} \frac{m_{\rm p}^{2/3}}{c\hbar^{1/2}} \frac{L_j^{1/2} v_w t^{1/3}}{\theta \dot{M}_d^{2/3}} \qquad (30)$$

Substituting jet power from eq (16) to eq. (30) we get

$$\frac{v_{\rm jh} - v_w}{v_r} = 20 \frac{v_{\rm w,-1}}{\theta_{-1} t_{0.3}^{2/3} \dot{M}_{d,-2}^{-1/6}}. \qquad (31)$$

We conclude that the jet-driven shock is radiatively dominated close to the break-out point.

In radiatively-dominated shocks the post-shock temperature T_s is determined by the condition

$$\frac{4\sigma_{SB}}{c}T_{\rm s}^4 \sim \rho_w(v_{\rm jh}-v_w)^2 = \frac{L_{\rm j}}{\pi(v_{\rm w}t\theta)^2 c}$$

$$T_{\rm s} = \frac{L_j^{1/4}}{(4\pi\sigma_{\rm SB})^{1/4}\sqrt{v_w t\theta}} \quad (32)$$

(Notice weak dependence of this estimate on the properties of the jet (power and opening angle), complete independence on the assumed mass loss rate of the disk, and only mild dependence on wind velocity.)

Substituting jet power from Eq. (16) we get

$$T_{\rm s} = 40\frac{M_{\rm d,-2}^{1/4}}{\theta_{-1}^{1/2}v_{\rm w,-1}^{1/2}t_{0.3}}\ {\rm keV} \quad (33)$$

where time t is time of shock breakout (estimate T_s is the upper limit since part of the energy incoming into the shock will be converted into bulk motion and into the production of pairs – these effects will reduce somewhat the post-shock temperature). At $t \sim$ few seconds, and given our order-of-magnitude approach, this estimate is very close to the observed temperature of the second prompt peak.

6.8. *Estimate of the viewing angle*

In the present model after the break out the collimated jet accelerates to highly relativistic velocities, and thus becomes highly de-beamed and not observable. Let's us estimate the constraints that observation place on the viewing angle.

The expected observed jet power of a relativistically boosted jet can be estimated as (see more details in Sikora et al. 1997)

$$L_{\rm obs} = \frac{\delta^3}{\Gamma_{\rm jet}}L_{\rm jet}, \quad (34)$$

here $\Gamma_{\rm jet}$ is Lorentz factor of the jet, $\delta = 1/[\Gamma_{\rm jet}(1 - v\cos\theta/c)]$ is Doppler factor of the jet, v is velocity of the jet and θ is an angle between observer and jet axis and $L_{\rm jet} = \chi L_{\rm BZ}$ is electromagnetic jet luminosity with efficiency χ. In the case of small angles ($|1-\cos\theta| \ll 1$, but θ can be $\gg 1/\Gamma_{\rm jet}$) we can write as $\Gamma_{\rm jet}/\delta = (\alpha^2+1)/2$ (Giannios et al. 2010; Aharonian et al. 2017), here $\alpha = \theta\Gamma_{\rm jet}$ and Eq (34) take a form:

$$\alpha = \left[\left(\frac{8\Gamma_{\rm jet}^2\chi L_{\rm BZ}}{L_{\rm obs}}\right)^{1/3} - 1\right]^{1/2}. \quad (35)$$

In the case of large viewing angles ($\alpha \gg 1$) the minimal viewing angle can be estimated as

$$\theta > \left(\frac{8\chi L_{\rm BZ}}{\Gamma_{\rm jet}^4 L_{\rm obs}}\right)^{1/6}. \quad (36)$$

Substituting parameters of the GRB 170817A to Eq. (36) we can estimate minimal viewing angle as

$$\theta > 0.3\left(\frac{\chi M_{\rm d0,-2}M_{\rm BH,0.5}^{1/3}t_{\rm vis,-1}^{2/3}}{\Gamma_{\rm jet,15}^4 L_{\rm obs,47.2}\alpha_{\rm ss,-1}h_{\rm d,-0.5}t_{0.3}^2}\right)^{1/6}. \quad (37)$$

The probability to do not observe such burst is $Prob \approx 1-\theta^2/2 \approx 1-0.05 \approx 0.95$.

Combining equations (14) and (35) we derive minimal observational angle and probability to observe the transient and present them on figure 9.

If we assume that the jet parameters of GRB170817A and GRB130603B are the same then using Equation (34) we obtain that $(\theta\Gamma)^6 \geq 30$. It is corroborate with the angular momentum and line of sight (~ 31 degrees) obtained from BNS coalescence LIGO Scientific Collaboration et al. (2017).

More detailed calculations of jet brightness from a viewing angle can be found in Kathirgamaraju et al. (2017); Lazzati et al. (2017).

7. CONCLUSIONS

In this paper, we discussed the results of the coordinated optical and radio search and optical observations of the LIGO/Fermi GBM event GW170817/GRB170817A. An optical transient of $\sim 19^m$ was detected by Chilescope observatory. The properties of the optical transient roughly match the kilonova activity. Importantly, the luminosity of a possible afterglow component of GRB170817A is at least 30 *times* less luminous than of GRB130603B afterglow at ~ 11 hours after burst onset. We provide upper limits on the possible short radio transient at 110 MHz associated with the GW170817/GRB170817A at the trigger time.

We discuss the prompt gamma-ray emission, consisting of a hard gamma-ray pulse followed by a soft tail, each delayed by ~ 2 seconds respect to the LIGO trigger. The appearance of the thermal component at the end of the burst is unusual for short GBRs. Both the hard pulse and the whole burst do not fit the Amati relation for short nor for long GRBs (Amati et al. 2002). This is especially true for the first hard pulse.

We then developed a theoretical model which must explain (i) a delay between the LIGO and Fermi triggers; (ii) the two-component nature of the prompt emission; (iii) the absence of early afterglows.

Delay between LIGO and Fermi signals. The delay between the LIGO and the EM signals depends both on the delayed switching-on of the BZ-powered jet and the jet propagation through the dense expanding envelope (see Eqns. (25) and (Gottlieb et al. (2017))). (The neutrino mechanism of jet launching is very sensitive to the disk temperature and should be more effective right after the disk formation; at this time the accretion rate is also maximal. On the other hand, the BZ mechanism is less sensitive to accretion rate and needs sufficient magnetic flux accumulated on the BH, (see *e.g.* Komissarov & Barkov 2009). Also, an operation of the BZ mechanism requires magnetically dominated plasma - the cleaning of polar regions of the BH can take time about a second (Barkov & Komissarov 2010).) We suggest the delay result from both activation of BZ-jet and the jet propagation through expanding envelope.

Two components of prompt emission. We suggest in our model that the two components come from, first, highly relativistic, nearly isotropic break out of a magnetized jet from the confining wind, and, the second one, from the wind material heated by the breaking-out jet. After activation of the BZ process, the jet head propagates through wind matter with subrelativistic veloc-

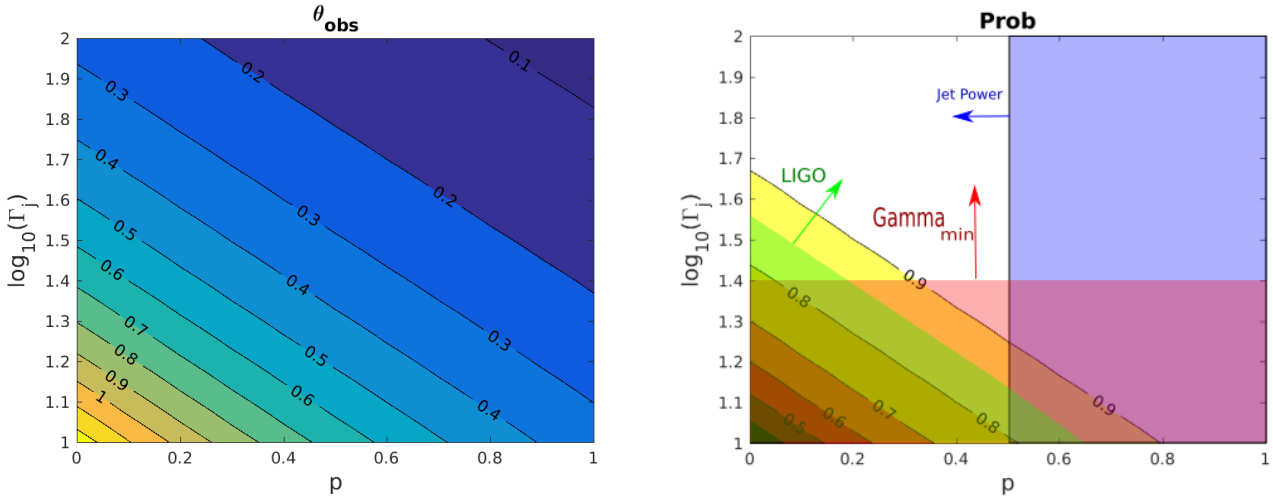

FIG. 9.— Observational angle (left) and probability to observe the transient (right) depends on wind parameter "p" and logarithm of jet Lorentz factor Γ_j. On the left plot we put limit on the minimal jet Lorentz factor (Eq.2) as pink aria and limitation on the wind "p" parameter from Eqs (26, 10 and 14) as purple aria. The green aria is follow from LIGO observations.

ity. The initially strongly magnetically-dominated jet partially transfers its magnetic energy into internal one, as discussed in §6.5. During the jet breaks out from the confining wind, the jet expands quasi-isotropically, see Fig. 7). The expanding matter accelerates up to the Lorentz factor (see Equation (2)) at the radius of $r_{\rm ha} \approx \Gamma_{\rm j,min} r_{\rm S} \approx 10^{10}$ cm where the cloud became transparent for radiation. The minimal variability time is $\sim r_s/c \sim 0.02$ s does not contradict the duration of the first hard pulse. We put a lower limit on the jet power (see Figure. 9) as $L_{\rm jet} \sim 10^{49}$erg s^{-1} (see equations (26, 10 and 16)).

Absence of early afterglows. We suggest that absence of the afterglow can be explained by the observer off-axis of the jet. After the jet breaks out a standard jet acceleration will be recovered - the BZ flow accelerates to $\Gamma \geq 25$, becomes internally causally disconnected and propagates ballistically. This acceleration will suppress the visibility of the BZ jet, and the corresponding forward shock.

The short-lived jet will launch a forward shock in the circumburst medium. (Only after sweeping large amount of the circumburst material, the evolution of the forward shock will become non-ballistic; this will occur at times much later than when $\Gamma \sim 1/\theta$ van Eerten & MacFadyen 2012; Lyutikov 2012). The observed jet luminosity, Eq. (34), in the case $\theta\Gamma_{\rm j} \gg 1$ gives

$$L_{\rm obs} \approx \frac{8}{\theta^6 \Gamma_{\rm jet}^4} L_{\rm jet}. \qquad (38)$$

Thus, as the jet accelerates it becomes dimmer (Tchekhovskoy et al. 2010; Komissarov et al. 2010; Lyutikov 2011a). The jet recovery time we can estimate as $2v_{\rm ex}t/c \approx 0.5$ s; this is close to duration of hard component and can be masked by it.

ACKNOWLEDGMENTS

ASP, PYuM, AAV, EDM are grateful to the Russian Science Foundation grant 15-12-30015. This work had been supported by NSF grant AST-1306672, DoE grant DE-SC0016369 and NASA grant 80NSSC17K0757. We acknowledge the excellent help in obtaining Chilescope data Sergei Pogrebsskiy and Ivan Rubzov.

REFERENCES

Aharonian, F. A., Barkov, M. V., & Khangulyan, D. 2017, ApJ, 841, 61
Allam, S., et al. 2017, GRB Coordinates Network, 21530, 1
Amati, L. 2010, arXiv:1002.2232
Amati, L., et al. 2002, A&A, 390, 81
Arcavi, I., et al. 2017, GRB Coordinates Network, 21538, 1
Baiotti, L., & Rezzolla, L. 2017, Reports on Progress in Physics, 80, 096901
Bardeen, J. M., Press, W. H., & Teukolsky, S. A. 1972, ApJ, 178, 347
Barkov, M. V. 2008, in American Institute of Physics Conference Series, Vol. 1054, American Institute of Physics Conference Series, ed. M. Axelsson, 79–85
Barkov, M. V., & Baushev, A. N. 2011, New Astr., 16, 46
Barkov, M. V., & Komissarov, S. S. 2008a, International Journal of Modern Physics D, 17, 1669
—. 2008b, MNRAS, 385, L28
—. 2010, MNRAS, 401, 1644
Barkov, M. V., & Pozanenko, A. S. 2011, MNRAS, 417, 2161
Beloborodov, A. M. 2003, ApJ, 588, 931
—. 2010, MNRAS, 407, 1033
—. 2017, ApJ, 838, 125
Beloborodov, A. M., & Mészáros, P. 2017, Space Sci. Rev., 207, 87
Beskin, V. S., & Nokhrina, E. E. 2006, MNRAS, 367, 375
Birkl, R., Aloy, M. A., Janka, H., & Müller, E. 2007, åp, 463, 51
Bisnovatyi-Kogan, G. S. 1970, AZh, 47, 813
Blandford, R. D., & Begelman, M. C. 1999, MNRAS, 303, L1
Blandford, R. D., & Znajek, R. L. 1977, MNRAS, 179, 433
Blinnikov, S. I., Novikov, I. D., Perevodchikova, T. V., & Polnarev, A. G. 1984, Pis ma Astronomicheskii Zhurnal, 10, 422
Brown, T. M., Baliber, N., & Bianco, F. B. 2013, PASP, 125, 1031, arXiv:1305.2437
Cash, W. 1979, ApJ, 228, 939
Connaughton, V., Blackburn, L., Briggs, M. S., Broida, J., & Burns, E. 2017, LVC GRB Coordinates Network, 21506
Coulter, D. A., Kilpatrick, C. D., Siebert, M. R., Foley, R. J., Shappee, B. J., Drout, M. R., Simon, J. S., & Piro, A. L. 2017, GRB Coordinates Network, 21529, 1
Dalya, G., Frei, Z., Galgoczi, G., Raffai, P., & de Souza, R. S. 2016, VizieR Online Data Catalog, 7275
D'Elia, V., Pian, E., Piranomonte, S., Branchesi, M., & Brocato, E. 2017, LVC GRB Coordinates Network, 21592
Derishev, E. V., Kocharovsky, V. V., & Kocharovsky, V. V. 1999, ApJ, 521, 640
Eichler, D., Livio, M., Piran, T., & Schramm, D. N. 1989a, Nature, 340, 126

—. 1989b, Nature, 340, 126
Ensman, L., & Burrows, A. 1992, ApJ, 393, 742
Giannios, D., Uzdensky, D. A., & Begelman, M. C. 2010, MNRAS, 402, 1649
Goldstein, A., Veres, P., & Burns, E. 2017, ApJL submitted
Goldstein, A., Veres, P., von Kienlin, A., Blackburn, L., & Briggs, M. S. 2017, LVC GRB Coordinates Network, 21528
Goodman, J. 1986, ApJ, 308, L47
Gottlieb, O., Nakar, E., & Piran, T. 2017, arXiv:1705.10797
Gralla, S. E., & Jacobson, T. 2014, MNRAS, 445, 2500
Gruber, D., et al. 2014, ApJS, 211, 12
Gruzinov, A. 1999, ArXiv:9902288
Johnson, M. H., & McKee, C. F. 1971, Phys. Rev. D, 3, 858
Kathirgamaraju, A., Barniol Duran, R., & Giannios, D. 2017, arXiv:1708.07488
Katz, B., Budnik, R., & Waxman, E. 2010, ApJ, 716, 781
Kennel, C. F., & Coroniti, F. V. 1984, ApJ, 283, 694
Komissarov, S. S. 2011, MNRAS, 418, L94
Komissarov, S. S., & Barkov, M. V. 2009, MNRAS, 397, 1153
—. 2010, MNRAS, 402, L25
Komissarov, S. S., Vlahakis, N., & Königl, A. 2010, MNRAS, 407, 17
Komissarov, S. S., Vlahakis, N., Königl, A., & Barkov, M. V. 2009, MNRAS, 394, 1182
Kompaneets, A. S. 1960, Soviet Physics Doklady, 5, 46
Lazzati, D., Lopez-Camara, D., Cantiello, M., Morsony, B. J., Perna, R., & Workman, J. C. 2017, arXiv:1709.01468
LeBlanc, J. M., & Wilson, J. R. 1970, ApJ, 161, 541
Li, L.-X., & Paczyński, B. 1998, ApJ, 507, L59
Lightman, A. P. 1982, ApJ, 253, 842
LIGO Scientific Collaboration, T., & Virgo Collaboration, T. 2017a, GRB Coordinates Network, 21505, 1
—. 2017b, GRB Coordinates Network, 21513, 1
—. 2017c, GRB Coordinates Network, 21509, 1
LIGO Scientific Collaboration, T., VIRGO Collaboration, T., Partner Astronomy Groups, Abbott, B. P., & et al. 2017, ApJ
Lipunov, V., et al. 2010, Advances in Astronomy, 2010, 349171
Lipunov, V. M., et al. 2017, GRB Coordinates Network, 21546, 1
Lithwick, Y., & Sari, R. 2001, ApJ, 555, 540
Lyutikov, M. 2006, New Journal of Physics, 8, 119
—. 2010, Phys. Rev. E, 82, 056305
—. 2011a, MNRAS, 411, 422
—. 2011b, Phys. Rev. D, 83, 124035
—. 2011c, Phys. Rev. D, 83, 064001
—. 2012, MNRAS, 421, 522
Lyutikov, M., & Hadden, S. 2012, Phys. Rev. E, 85, 026401
Lyutikov, M., & Usov, V. V. 2000, ApJ, 543, L129
McKinney, J. C., Tchekhovskoy, A., & Blandford, R. D. 2012, MNRAS, 423, 3083
Metzger, B. D., Piro, A. L., & Quataert, E. 2008a, MNRAS, 390, 781
Metzger, B. D., Quataert, E., & Thompson, T. A. 2008b, MNRAS, 385, 1455
Metzger, B. D., et al. 2010, MNRAS, 406, 2650
Minaev, P. Y., & Pozanenko, A. S. 2017, Astronomy Letters, 43, 1
Minaev, P. Y., Pozanenko, A. S., & Loznikov, V. M. 2010, Astronomy Letters, 36, 707
Minaev, P. Y., Pozanenko, A. S., Molkov, S. V., & Grebenev, S. A. 2014, Astronomy Letters, 40, 235
Moharana, R., & Piran, T. 2017, arXiv:1705.02598
Nakar, E., & Sari, R. 2012, ApJ, 747, 88
Paczynski, B. 1986a, ApJ, 308, L43
—. 1986b, ApJ, 308, L43
—. 1990, ApJ, 363, 218
Porth, O., Komissarov, S. S., & Keppens, R. 2013, MNRAS, 431, L48
—. 2014, MNRAS, 438, 278
Pozanenko, A., Mazaeva, E., Volnova, A., Minaev, P., & Krugov, M. 2017a, GRB Coordinates Network, 21618, 1
Pozanenko, A., Volnova, A. Mazaeva, E., Minaev, P., & Krugov, M. 2017b, GRB Coordinates Network, 21635, 1
—. 2017c, GRB Coordinates Network, 21644, 1
Pozanenko, A., Volnova, A. Mazaeva, E., Minaev, P., Moskvitin, A., & Krugov, M. 2017d, GRB Coordinates Network, 21898, 1
Qin, Y.-P., & Chen, Z.-F. 2013, MNRAS, 430, 163
Radice, D., Galeazzi, F., Lippuner, J., Roberts, L. F., Ott, C. D., & Rezzolla, L. 2016, MNRAS, 460, 3255
Rees, M. J., & Gunn, J. E. 1974, MNRAS, 167, 1
Rees, M. J., & Mszros, P. 2005, The Astrophysical Journal, 628, 847
Rezzolla, L., Giacomazzo, B., Baiotti, L., Granot, J., Kouveliotou, C., & Aloy, M. A. 2011, ApJ, 732, L6
Ruiz, M., Lang, R. N., Paschalidis, V., & Shapiro, S. L. 2016, ApJ, 824, L6
Samodurov, V. A., et al. 2017, in Data Analytics and Management in Data Intensive Domains. DAMDID/RCDL 2016. Communications in Computer and Information Science, ed. M. Y. Kalinichenko L., Kuznetsov S., Vol. 706
Savchenko, V., Ferrigno, C., & Kuulkers, E. 2017, ApJL submitted
Savchenko, V., Mereghetti, S., Ferrigno, C., Kuulkers, E., & Bazzano, A. 2017, LVC GRB Coordinates Network, 21507
Schlafly, E. F., & Finkbeiner, D. P. 2011, ApJ, 737, 103
Shakura, N. I., & Sunyaev, R. A. 1973, A&A, 24, 337
Sikora, M., Madejski, G., Moderski, R., & Poutanen, J. 1997, ApJ, 484, 108
Svensson, R. 1982, ApJ, 258, 335
Svinkin, D. S., et al. 2016, ApJS, 224, 10
Tan, J. C., Matzner, C. D., & McKee, C. F. 2001, ApJ, 551, 946
Tanvir, N. R., Levan, A. J., Fruchter, A. S., Hjorth, J., Hounsell, R. A., Wiersema, K., & Tunnicliffe, R. L. 2013, Nature, 500, 547
Tanvir, N. R., & Levan, A. J. 2017, GRB Coordinates Network, 21544
Tchekhovskoy, A., Narayan, R., & McKinney, J. C. 2010, New Astr., 15, 749
Usov, V. V. 1992, Nature, 357, 472
van Eerten, H. J., & MacFadyen, A. I. 2012, ApJ, 751, 155
Viganò, D., & Mereghetti, S. 2009, in The Extreme Sky: Sampling the Universe above 10 keV
Volnova, A. A., et al. 2014, MNRAS, 442, 2586
von Kienlin, A., Meegan, C., & Goldstein, A. 2017, GRB Coordinates Network, 21520, 1
von Kienlin, A., et al. 2003, A&A, 411, L299
—. 2014, ApJS, 211, 13
Weaver, T. A. 1976, ApJS, 32, 233
Yang, S., Valenti, S., Sand, D., Tartaglia, L., Cappellaro, E., Reichart, D., Haislip, J., & Kouprianov, V. 2017, GRB Coordinates Network, 21531, 1
Zalamea, I., & Beloborodov, A. M. 2011, MNRAS, 410, 2302

APPENDIX

A. EARLY OPTICAL OBSERVATIONS OF CHILESCOPE OBSERVATORY

A.1. *CHILESCOPE*

CHILESCOPE[4] is a remote control commercial observatory located in the Chilean Andes (W 70.75 S 30.27) equipped with two identical 50 cm fast Newton astrographs (Newtonian 1 ASA-500 and Newtonian 2) and 1-meter Ritchey Chretien telescope (RC-1000).

Both Newtonians with f/3.8 are on "Z" equatorial mounts, both are equipped with 4K×4K FLI PROLINE 16803 CCD cameras with Astrodon Generation 2 E-Series Luminance filter [5], which is approximately equivalent to a clear light. The field of view is 67×67 arcminutes.

1-meter RC-1000 telescope is mounted on an alt-azimuth mount with direct drives on both axis and has a focal ratio f/6.8 with a reducer. The telescope is also equipped with 4K×4K FLI PROLINE 16803 CCD camera with Astrodon Generation 2 E-Series Luminance filter. The resulting field of view is 18.6×18.6 arcminutes. It also has a good thermal stabilization with the working temperature of -30 degrees Celsius.

[4] http://www.chilescope.com/

[5] https://www.cloudynights.com/uploads/monthly_09_2014/post-23216-0-17456300-1411330347.jpg

TABLE 5
TELESCOPES.

Telescope	Field of view	Number of images
RC-1000	18.6′x 18.6′	48
ASA-500	67′x 67′	76

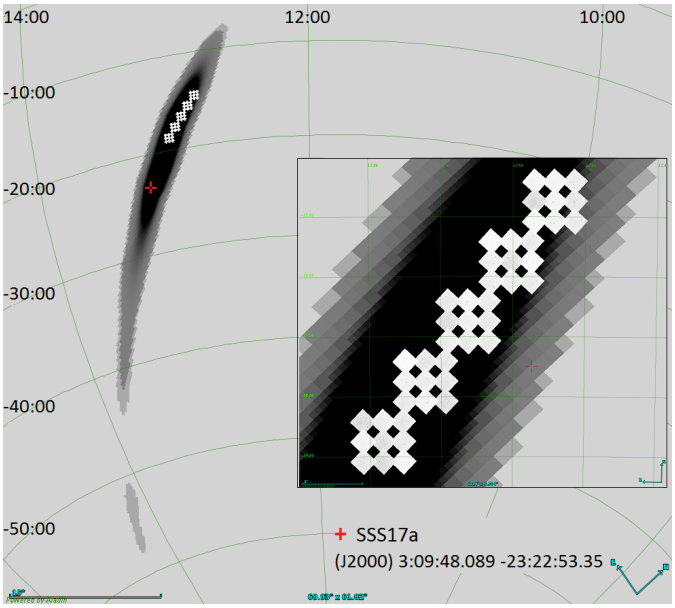

FIG. 10.— Observations of RC-1000 telescope. The figure shows LIGO/Virgo localization with partial covering this area by RC-1000 telescope. Observations of RC-1000 telescope began 11.1 hours since GW trigger. Red target marks optical counterpart of a GW signal named as SSS17a (RA(J2000)=03:09:48.089, Dec.(J2000)=-23:22:53.35).

A.2. *Chronology*

We observed the field of LIGO/Virgo trigger G298048 (LIGO Scientific Collaboration & Virgo Collaboration 2017c,b) and the error box of Fermi/GBM short burst GRB 170817A (Connaughton et al. 2017) with RC-1000 and ASA-500 telescopes of CHILESCOPE observatory[6].The observations started on Aug 17 (UT) 23:17:16 in *Lum* filter. The last image was recorded on Aug 18 (UT) 00:59:57.

A.3. *Observations of RC-1000 telescope*

RC-1000 covered central part of G298048 localization with typical limiting magnitude of 20^m at 60 s exposure in each image. 48 images were obtained, but some images have the same coordinates. Date UT and center of each image see in Tab 6.

The optical counterpart candidate was independently discovered by six teams (Coulter et al. 2017; Yang et al. 2017; Tanvir & Levan 2017; Lipunov et al. 2017; Allam et al. 2017; Arcavi et al. 2017) with the first announcement at 01:05 UT Aug 18 (12.4 hours since GW trigger and 25.6 minutes minutes after the end of RC-1000 telescope observations) is out of the coverage in the first epoch of the observations. The covering map can be found in Fig. 10.

A.4. *Observations of ASA-500 telescope*

We also covered northern part of GBM/Fermi localization 1-sigma containment, statistical only (Connaughton et al. 2017). The coverage of the GBM localization is about 16 %. Typical limiting magnitude of 17.5^m at 60 s exposure in each image. Totally was obtained 76 images. Date UT and center of each image see in Tab 7. The covering map can be found in Fig. 11.

B. MAGNETIC FORCE-FREE BOMB

At the moment of the break-out the jet, which was strongly magnetically dominated close to the BH, but became mildly magnetically dominated during the confined propagation, §6.5, starts to expand and accelerate. As the pair density falls precipitously, the flow becomes more and more magnetically dominated. In this appendix we consider the explanation of a magnetic force-free bomb – radial motion of the post-break-out highly magnetized plasma flows.

Consider radial expansion of force-free plasma carrying toroidal magnetic field. Relativistic force-free condition implies that the total EM force vanishes (Gruzinov 1999)

$$\mathbf{E}\,\mathrm{div}\,\mathbf{E}+\mathbf{J}\times\mathbf{B}=0\rightarrow\mathbf{J}=\frac{(\mathbf{E}\times\mathbf{B})\nabla\cdot\mathbf{E}+(\mathbf{B}\cdot\nabla\times\mathbf{B}-\mathbf{E}\cdot\nabla\times\mathbf{E})\mathbf{B}}{B^2}, \tag{B1}$$

[6] http://www.chilescope.com

TABLE 6
Observations of RC-1000 telescope

UT date	Time since GW trigger (days)	Center (RA)	Center (Dec.)
2017-08-17 23:44:31	0.46108	12 ^{h} 48 ^{m} 28.414 ^{s}	-14 °25 ′07.037 ″
2017-08-17 23:45:53	0.46203	12 ^{h} 47 ^{m} 05.895 ^{s}	-14 °25 ′04.261 ″
2017-08-17 23:47:16	0.46299	12 ^{h} 45 ^{m} 43.416 ^{s}	-14 °25 ′01.827 ″
2017-08-17 23:48:38	0.46394	12 ^{h} 48 ^{m} 28.594 ^{s}	-14 °45 ′01.452 ″
2017-08-17 23:50:00	0.46488	12 ^{h} 47 ^{m} 05.988 ^{s}	-14 °44 ′59.153 ″
2017-08-17 23:51:23	0.46584	12 ^{h} 45 ^{m} 43.329 ^{s}	-14 °44 ′57.545 ″
2017-08-17 23:52:45	0.46679	12 ^{h} 48 ^{m} 28.701 ^{s}	-15 °04 ′58.286 ″
2017-08-17 23:54:07	0.46774	12 ^{h} 47 ^{m} 05.854 ^{s}	-15 °04 ′58.530 ″
2017-08-17 23:55:30	0.46870	12 ^{h} 45 ^{m} 43.005 ^{s}	-15 °04 ′59.031 ″
2017-08-17 23:58:01	0.47045	12 ^{h} 51 ^{m} 28.799 ^{s}	-15 °25 ′03.691 ″
2017-08-17 23:59:23	0.47140	12 ^{h} 50 ^{m} 05.874 ^{s}	-15 °25 ′02.099 ″
2017-08-18 00:00:46	0.47236	12 ^{h} 48 ^{m} 42.901 ^{s}	-15 °25 ′00.518 ″
2017-08-18 00:02:17	0.47341	12 ^{h} 51 ^{m} 28.942 ^{s}	-15 °45 ′00.766 ″
2017-08-18 00:03:49	0.47448	12 ^{h} 50 ^{m} 05.842 ^{s}	-15 °44 ′59.895 ″
2017-08-18 00:05:22	0.47556	12 ^{h} 48 ^{m} 42.695 ^{s}	-15 °44 ′56.860 ″
2017-08-18 00:06:53	0.47661	12 ^{h} 51 ^{m} 28.907 ^{s}	-16 °04 ′59.101 ″
2017-08-18 00:08:15	0.47756	12 ^{h} 50 ^{m} 05.657 ^{s}	-16 °04 ′57.618 ″
2017-08-18 00:09:38	0.47852	12 ^{h} 48 ^{m} 42.360 ^{s}	-16 °04 ′57.688 ″
2017-08-18 00:13:16	0.48104	12 ^{h} 51 ^{m} 28.630 ^{s}	-15 °25 ′05.288 ″
2017-08-18 00:14:38	0.48199	12 ^{h} 50 ^{m} 05.706 ^{s}	-15 °25 ′02.368 ″
2017-08-18 00:17:15	0.48381	12 ^{h} 54 ^{m} 29.036 ^{s}	-16 °25 ′02.125 ″
2017-08-18 00:18:50	0.48491	12 ^{h} 54 ^{m} 29.003 ^{s}	-16 °25 ′03.603 ″
2017-08-18 00:20:21	0.48596	12 ^{h} 53 ^{m} 05.630 ^{s}	-16 °25 ′02.356 ″
2017-08-18 00:21:52	0.48701	12 ^{h} 51 ^{m} 42.259 ^{s}	-16 °25 ′00.875 ″
2017-08-18 00:23:22	0.48806	12 ^{h} 54 ^{m} 29.055 ^{s}	-16 °45 ′00.484 ″
2017-08-18 00:24:53	0.48911	12 ^{h} 53 ^{m} 05.560 ^{s}	-16 °44 ′58.705 ″
2017-08-18 00:26:26	0.49019	12 ^{h} 51 ^{m} 41.997 ^{s}	-16 °44 ′57.424 ″
2017-08-18 00:27:57	0.49124	12 ^{h} 54 ^{m} 29.024 ^{s}	-17 °04 ′59.058 ″
2017-08-18 00:29:20	0.49220	12 ^{h} 53 ^{m} 05.393 ^{s}	-17 °04 ′59.049 ″
2017-08-18 00:30:42	0.49315	12 ^{h} 51 ^{m} 41.709 ^{s}	-17 °04 ′58.549 ″
2017-08-18 00:34:03	0.49547	12 ^{h} 57 ^{m} 29.158 ^{s}	-17 °25 ′03.586 ″
2017-08-18 00:35:33	0.49652	12 ^{h} 56 ^{m} 05.408 ^{s}	-17 °25 ′02.790 ″
2017-08-18 00:37:04	0.49757	12 ^{h} 54 ^{m} 41.653 ^{s}	-17 °24 ′59.856 ″
2017-08-18 00:38:26	0.49852	12 ^{h} 57 ^{m} 29.218 ^{s}	-17 °45 ′01.451 ″
2017-08-18 00:39:49	0.49948	12 ^{h} 56 ^{m} 05.305 ^{s}	-17 °44 ′59.001 ″
2017-08-18 00:41:19	0.50052	12 ^{h} 54 ^{m} 41.310 ^{s}	-17 °44 ′57.055 ″
2017-08-18 00:42:50	0.50157	12 ^{h} 57 ^{m} 29.230 ^{s}	-18 °04 ′59.511 ″
2017-08-18 00:44:13	0.50253	12 ^{h} 56 ^{m} 05.075 ^{s}	-18 °04 ′58.201 ″
2017-08-18 00:45:35	0.50348	12 ^{h} 54 ^{m} 40.882 ^{s}	-18 °04 ′57.991 ″
2017-08-18 00:48:13	0.50531	13 ^{h} 00 ^{m} 29.457 ^{s}	-18 °25 ′01.845 ″
2017-08-18 00:49:43	0.50635	12 ^{h} 59 ^{m} 05.148 ^{s}	-18 °25 ′01.236 ″
2017-08-18 00:51:06	0.50731	12 ^{h} 57 ^{m} 40.809 ^{s}	-18 °24 ′59.051 ″
2017-08-18 00:52:28	0.50826	13 ^{h} 00 ^{m} 29.458 ^{s}	-18 °44 ′59.417 ″
2017-08-18 00:53:50	0.50921	12 ^{h} 59 ^{m} 04.993 ^{s}	-18 °44 ′57.667 ″
2017-08-18 00:55:23	0.51029	12 ^{h} 57 ^{m} 40.424 ^{s}	-18 °44 ′56.776 ″
2017-08-18 00:56:54	0.51134	13 ^{h} 00 ^{m} 29.415 ^{s}	-19 °04 ′57.375 ″
2017-08-18 00:58:25	0.51240	12 ^{h} 59 ^{m} 04.778 ^{s}	-19 °04 ′57.208 ″
2017-08-18 00:59:57	0.51346	12 ^{h} 57 ^{m} 40.097 ^{s}	-19 °04 ′55.261 ″

(for GR formulation see Lyutikov 2011c; Komissarov 2011).

Separating the angular and the time-radial dependence, $B_\phi = B_\phi(t,r)b_\phi(\theta)$ and $E_\theta = E_\theta(t,r)e_\theta(\theta)$ we find two types

TABLE 7
Observations of ASA-500 telescope

UT date	Time since GW trigger (days)	Center (RA)	Center (Dec.)
2017-08-17 23:17:16	0.44215	12 ^{h} 30 ^{m} 15.598 ^{s}	-30 °12 ′47.661 ″
2017-08-17 23:18:42	0.44315	12 ^{h} 25 ^{m} 37.552 ^{s}	-30 °12 ′46.982 ″
2017-08-17 23:20:08	0.44414	12 ^{h} 20 ^{m} 59.825 ^{s}	-30 °12 ′51.272 ″
2017-08-17 23:21:34	0.44514	12 ^{h} 16 ^{m} 22.006 ^{s}	-30 °12 ′54.690 ″
2017-08-17 23:23:00	0.44613	12 ^{h} 11 ^{m} 44.220 ^{s}	-30 °12 ′56.952 ″
2017-08-17 23:24:26	0.44713	12 ^{h} 07 ^{m} 06.472 ^{s}	-30 °12 ′59.341 ″
2017-08-17 23:25:51	0.44811	12 ^{h} 02 ^{m} 28.537 ^{s}	-30 °13 ′04.766 ″
2017-08-17 23:27:08	0.44900	11 ^{h} 57 ^{m} 50.769 ^{s}	-30 °13 ′06.317 ″
2017-08-17 23:28:26	0.44991	11 ^{h} 53 ^{m} 12.785 ^{s}	-30 °13 ′12.156 ″
2017-08-17 23:29:51	0.45089	11 ^{h} 48 ^{m} 34.883 ^{s}	-30 °13 ′16.196 ″
2017-08-17 23:31:09	0.45179	11 ^{h} 43 ^{m} 56.993 ^{s}	-30 °13 ′19.841 ″
2017-08-17 23:32:26	0.45269	11 ^{h} 38 ^{m} 46.482 ^{s}	-31 °13 ′44.353 ″
2017-08-17 23:33:51	0.45367	11 ^{h} 34 ^{m} 41.269 ^{s}	-30 °13 ′27.977 ″
2017-08-17 23:35:09	0.45457	11 ^{h} 30 ^{m} 03.364 ^{s}	-30 °13 ′34.495 ″
2017-08-17 23:36:26	0.45546	11 ^{h} 25 ^{m} 25.436 ^{s}	-30 °13 ′37.753 ″
2017-08-17 23:37:51	0.45645	11 ^{h} 20 ^{m} 47.749 ^{s}	-30 °13 ′41.649 ″
2017-08-17 23:39:16	0.45743	11 ^{h} 16 ^{m} 09.869 ^{s}	-30 °13 ′48.310 ″
2017-08-17 23:40:34	0.45833	11 ^{h} 11 ^{m} 31.887 ^{s}	-30 °13 ′52.435 ″
2017-08-17 23:41:51	0.45922	11 ^{h} 06 ^{m} 54.122 ^{s}	-30 °13 ′57.672 ″
2017-08-17 23:43:16	0.46021	11 ^{h} 02 ^{m} 16.046 ^{s}	-30 °14 ′03.015 ″
2017-08-17 23:44:34	0.46111	12 ^{h} 30 ^{m} 15.005 ^{s}	-30 °13 ′04.766 ″
2017-08-17 23:45:51	0.46200	12 ^{h} 25 ^{m} 33.996 ^{s}	-31 °13 ′07.322 ″
2017-08-17 23:47:17	0.46300	12 ^{h} 20 ^{m} 53.256 ^{s}	-31 °13 ′10.210 ″
2017-08-17 23:48:43	0.46399	12 ^{h} 16 ^{m} 12.320 ^{s}	-31 °13 ′11.223 ″
2017-08-17 23:50:09	0.46499	12 ^{h} 11 ^{m} 31.649 ^{s}	-31 °13 ′15.275 ″
2017-08-17 23:51:36	0.46600	12 ^{h} 06 ^{m} 50.885 ^{s}	-31 °13 ′18.115 ″
2017-08-17 23:53:02	0.46699	12 ^{h} 02 ^{m} 10.096 ^{s}	-31 °13 ′24.372 ″
2017-08-17 23:54:28	0.46799	11 ^{h} 57 ^{m} 29.387 ^{s}	-31 °13 ′26.510 ″
2017-08-17 23:55:45	0.46888	11 ^{h} 52 ^{m} 48.745 ^{s}	-31 °13 ′31.809 ″
2017-08-17 23:57:02	0.46977	11 ^{h} 48 ^{m} 07.899 ^{s}	-31 °13 ′33.279 ″
2017-08-17 23:58:28	0.47076	11 ^{h} 43 ^{m} 27.248 ^{s}	-31 °13 ′38.379 ″
2017-08-17 23:59:53	0.47175	11 ^{h} 38 ^{m} 12.086 ^{s}	-32 °14 ′00.137 ″
2017-08-18 00:01:18	0.47273	11 ^{h} 34 ^{m} 05.570 ^{s}	-31 °13 ′47.746 ″
2017-08-18 00:02:35	0.47362	11 ^{h} 29 ^{m} 24.922 ^{s}	-31 °13 ′51.547 ″
2017-08-18 00:04:00	0.47461	11 ^{h} 24 ^{m} 44.156 ^{s}	-31 °13 ′57.384 ″
2017-08-18 00:05:18	0.47551	11 ^{h} 20 ^{m} 03.402 ^{s}	-31 °14 ′02.252 ″
2017-08-18 00:06:35	0.47640	11 ^{h} 15 ^{m} 22.440 ^{s}	-31 °14 ′06.208 ″
2017-08-18 00:08:00	0.47738	11 ^{h} 10 ^{m} 41.821 ^{s}	-31 °14 ′09.616 ″
2017-08-18 00:09:18	0.47829	11 ^{h} 06 ^{m} 01.019 ^{s}	-31 °14 ′16.647 ″
2017-08-18 00:10:35	0.47918	11 ^{h} 01 ^{m} 20.029 ^{s}	-31 °14 ′19.995 ″
2017-08-18 00:12:05	0.48022	12 ^{h} 30 ^{m} 13.856 ^{s}	-32 °13 ′21.158 ″
2017-08-18 00:13:23	0.48112	12 ^{h} 25 ^{m} 30.032 ^{s}	-32 °13 ′23.827 ″
2017-08-18 00:14:40	0.48201	12 ^{h} 20 ^{m} 46.426 ^{s}	-32 °13 ′25.644 ″
2017-08-18 00:16:06	0.48301	12 ^{h} 16 ^{m} 02.484 ^{s}	-32 °13 ′29.700 ″
2017-08-18 00:17:23	0.48390	12 ^{h} 11 ^{m} 18.718 ^{s}	-32 °13 ′32.247 ″
2017-08-18 00:18:40	0.48479	12 ^{h} 06 ^{m} 35.049 ^{s}	-32 °13 ′34.391 ″
2017-08-18 00:19:58	0.48569	12 ^{h} 01 ^{m} 51.128 ^{s}	-32 °13 ′39.111 ″
2017-08-18 00:21:15	0.48659	11 ^{h} 57 ^{m} 07.348 ^{s}	-32 °13 ′43.128 ″
2017-08-18 00:22:32	0.48748	11 ^{h} 52 ^{m} 23.580 ^{s}	-32 °13 ′47.111 ″
2017-08-18 00:23:57	0.48846	11 ^{h} 47 ^{m} 39.710 ^{s}	-32 °13 ′50.407 ″
2017-08-18 00:25:15	0.48936	11 ^{h} 42 ^{m} 56.111 ^{s}	-32 °13 ′54.176 ″

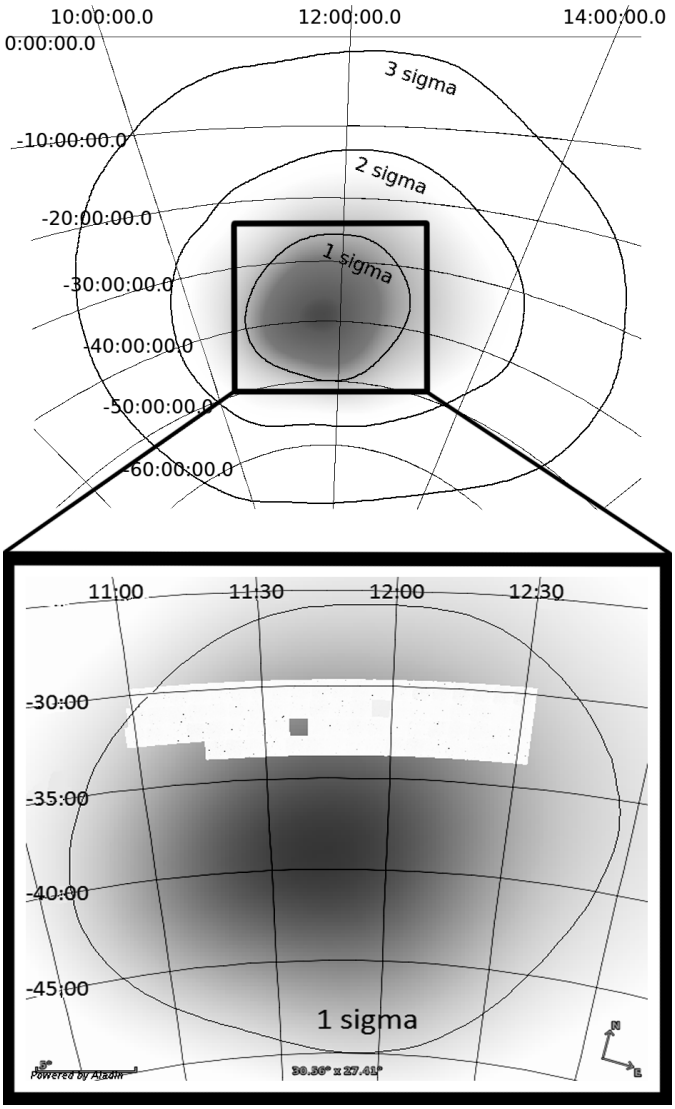

FIG. 11.— Observations of ASA-500 telescope. GRB 170817A localization estimate from Fermi/GBM data alone is shown in the upper panel. ASA-500 telescope covering of the part of 1 sigma Fermi/GBM localization is shown in the bottom panel. Observations of ASA-500 telescope began 10.6 hours after GW trigger.

of solution. The first is the solution self-similar in $Z = r/t$,

$$
\begin{aligned}
&E_\theta(Z) = B_\phi(Z) = (1 - 1/Z)B_0 \\
&e_\theta(\theta) = b_\phi(\theta) \\
&j_r = (1 - 1/Z)\frac{\partial_\theta(b_\phi \sin\theta)}{r \sin\theta} \\
&\mathrm{div}\,\mathbf{E} = (1 - 1/Z)\frac{\partial_\theta(b_\phi \sin\theta)}{r \sin\theta} = j_r
\end{aligned}
\tag{B2}
$$

Equations (B2) represent solutions for the polar-angle-dependent expansion of force-free plasma into vacuum. Poynting flux is zero at the edge of the outflow at $r = t$ and increases for smaller r. If the source is located at $r \ll t$, it is required that the source luminosity increases with time $\propto t^2$ for the solution to be applicable.

Second, looking for solution of the type $B_\phi, E_\theta \propto 1/r$, we find that the following scaling satisfies the Maxwell equations

$$
\begin{aligned}
&B_\phi(t, r) = E_\theta(t, r) = \frac{f(t - r)}{r} \\
&j_r = \frac{f(t - r)}{r^2}\frac{\partial_\theta(b_\phi \sin\theta)}{r \sin\theta}
\end{aligned}
\tag{B3}
$$

where f is an arbitrary function of the argument. This solution represent a force-free pulse of initial shape $f(r)$ moving

TABLE 8
Observations of ASA-500 telescope, continued

UT date	Time since GW trigger (days)	Center (RA)	Center (Dec.)
2017-08-18 00:27:57	0.49124	11 ^{h} 33 ^{m} 28.248 ^{s}	-32 °14 ′05.578 ″
2017-08-18 00:29:22	0.49222	11 ^{h} 28 ^{m} 44.497 ^{s}	-32 °14 ′08.661 ″
2017-08-18 00:30:39	0.49311	11 ^{h} 24 ^{m} 00.649 ^{s}	-32 °14 ′14.154 ″
2017-08-18 00:31:57	0.49402	11 ^{h} 19 ^{m} 16.820 ^{s}	-32 °14 ′20.406 ″
2017-08-18 00:33:14	0.49491	11 ^{h} 14 ^{m} 32.974 ^{s}	-32 °14 ′23.645 ″
2017-08-18 00:34:31	0.49580	11 ^{h} 09 ^{m} 49.015 ^{s}	-32 °14 ′27.265 ″
2017-08-18 00:35:58	0.49681	11 ^{h} 05 ^{m} 05.077 ^{s}	-32 °14 ′30.945 ″
2017-08-18 00:37:24	0.49780	11 ^{h} 00 ^{m} 21.126 ^{s}	-32 °14 ′35.378 ″
2017-08-18 00:38:54	0.49884	12 ^{h} 30 ^{m} 13.123 ^{s}	-33 °13 ′39.301 ″
2017-08-18 00:40:21	0.49985	12 ^{h} 25 ^{m} 26.171 ^{s}	-33 °13 ′37.855 ″
2017-08-18 00:41:38	0.50074	12 ^{h} 20 ^{m} 38.975 ^{s}	-33 °13 ′44.215 ″
2017-08-18 00:42:55	0.50163	12 ^{h} 15 ^{m} 52.081 ^{s}	-33 °13 ′45.463 ″
2017-08-18 00:44:12	0.50252	12 ^{h} 11 ^{m} 05.080 ^{s}	-33 °13 ′48.273 ″
2017-08-18 00:45:38	0.50352	12 ^{h} 06 ^{m} 18.116 ^{s}	-33 °13 ′51.389 ″
2017-08-18 00:47:04	0.50451	12 ^{h} 01 ^{m} 31.219 ^{s}	-33 °13 ′57.070 ″
2017-08-18 00:48:30	0.50551	11 ^{h} 56 ^{m} 44.050 ^{s}	-33 °14 ′00.839 ″
2017-08-18 00:49:56	0.50650	11 ^{h} 51 ^{m} 56.967 ^{s}	-33 °14 ′04.169 ″
2017-08-18 00:51:21	0.50749	11 ^{h} 47 ^{m} 10.057 ^{s}	-33 °14 ′07.798 ″
2017-08-18 00:52:47	0.50848	11 ^{h} 39 ^{m} 19.229 ^{s}	-30 °13 ′24.617 ″
2017-08-18 00:52:47	0.50848	11 ^{h} 42 ^{m} 22.994 ^{s}	-33 °14 ′11.486 ″
2017-08-18 00:54:13	0.50948	11 ^{h} 37 ^{m} 35.838 ^{s}	-33 °14 ′16.286 ″
2017-08-18 00:55:39	0.51047	11 ^{h} 32 ^{m} 49.002 ^{s}	-33 °14 ′20.323 ″
2017-08-18 00:57:05	0.51147	11 ^{h} 28 ^{m} 01.904 ^{s}	-33 °14 ′23.832 ″
2017-08-18 00:58:31	0.51247	11 ^{h} 23 ^{m} 14.613 ^{s}	-33 °14 ′28.525 ″
2017-08-18 00:59:48	0.51336	11 ^{h} 18 ^{m} 27.436 ^{s}	-33 °14 ′32.516 ″

with the speed of light – a force-free bomb.

Both solutions (B2) and (B3) are different from EM fields in vacuum since there are non-zero currents and charge densities in the flow. A general time-dependent approach to force-free fields for the specific case of $\rho = j$ has been discussed by Gralla & Jacobson (2014); see Lyutikov (2011b) for a related time-dependent solution in general relativity.